https://doi.org/10.5194/egusphere-2026-6552
Preprint. Discussion started: 13 November 2026
© Author(s) 2026. CC BY 4.0 License.

Dynamical characterisation of past and future changes in the Atlantic meridional overturning circulation from CMIP6

Théophile Caby[1], Florian Sévellec[1], and Arthur Coquereau[2]

[1]Laboratoire d'Océanographie Physique et Spatiale, Univ Brest CNRS IRD Ifremer, Brest, France
[2]Environnements et Paléoenvironnements Océaniques et Continentaux (EPOC), Université de Bordeaux, Pessac, France

Correspondence: Théophile Caby (theophile.caby@univ-brest.fr)

Abstract. The Atlantic Meridional Overturning Circulation (AMOC) is a leading candidate tipping element, yet most evidence for its destabilisation rests on critical slowing down indicators applied to scalar time series. Here we instead treat a high dimensional slice of the circulation state as a dynamical system, using ACCESS-ESM1.5 CMIP6 ensembles from 1850 to 2300 under a low, an intermediate, a high, and an overshoot forcing pathway. A low dimensional embedding by uniform manifold approximation and projection (UMAP) shows whether the circulation stays in one dynamical regime or moves between several. We check it against the local dimension of the attractor, computed in the original phase space, and the two diagnostics agree. Under high forcing, the circulation moves permanently to a new regime via a lower dimensional intermediate stage, which is a change in the dynamics and not only a weakening. Under intermediate forcing, it has reached that intermediate stage by 2100. Under low forcing and under overshoot, it is displaced but returns to its original regime once CO_2 declines, so in this model the overshoot is a safe one. We discuss the implications for assessments of AMOC stability and for overshoot pathways.

1 Introduction

The Atlantic Meridional Overturning Circulation carries warm, salty surface water northward across the Atlantic and returns cold, deep water southward. In doing so, it moves a substantial fraction of the global ocean heat transport, and it shapes the climate of the North Atlantic sector (Ganachaud and Wunsch, 2000; Rahmstorf et al., 2015; Trenberth and Fasullo, 2017; Johns et al., 2023). The AMOC is also one of the most frequently cited large scale tipping elements of the Earth system (Lenton et al., 2008; Armstrong McKay et al., 2022). Idealised and coupled models alike suggest that it can, in principle, support more than one stable mode of operation (consistently with the pioneer idealised model of Stommel, 1961, or more recent versions Sévellec and Fedorov, 2014, and Sévellec and Fedorov, 2016). Paleo-oceanographic studies of the last glacial period have described large amplitude climate events linked to such AMOC regime changes (Dansgaard et al., 1993; McManus et al., 2004; Böhm et al., 2015; Henry and McManus, 2016; Sévellec and Fedorov, 2014). These switches are suspected to cause abrupt climate changes (Boers, 2021; van Westen et al., 2024), notably because of the important reorganisation of the North Atlantic ocean heat transport between the two AMOC states (e.g., Sévellec and Fedorov, 2011). Because of its central role and major impact on the climate, the AMOC has been continuously monitored in the subtropical basin since 2004 (RAPID array at 26.5° N, Moat et al., 2024) and in the subpolar basin since 2014 (OSNAP array, Fu et al., 2023). These networks are also supplemented by

https://doi.org/10.5194/egusphere-2026-6552
Preprint. Discussion started: 13 November 2026
© Author(s) 2026. CC BY 4.0 License.

repeated oceanographic expeditions (e.g. OVIDE, Mercier et al., 2015, 2024). AMOC in-situ observations present a significant slowdown event around 2010, suspected to be partly linked to a decrease of the wind forcing. Recent studies have identified a change point around this event (Moat et al., 2020; Johns et al., 2023), with a weaker AMOC afterward. This aligns with the hypothesis of ongoing changes of the AMOC, supported by in situ measurements of the subpolar AMOC and the North Atlantic Deep Western Boundary Current from the OSNAP mooring array, despite the shorter duration of these observations (i.e., 2014-2020, Koman et al., 2024). Proxy observations enabling us to go further back in time have recently suggested an ongoing weakening of AMOC (Caesar et al., 2018), although their confidence levels remain low (Fox-Kemper et al., 2021) and other recent studies based on reconstructions do not report such a decline (Terhaar et al., 2025). Statistical early warning analyses of sea surface temperature and salinity fingerprints report a loss of resilience consistent with an approach toward a critical transition (Boulton et al., 2014; Boers, 2021), and at least one study proposes a central estimate for the timing of a possible collapse within this century (Ditlevsen and Ditlevsen, 2023); physics-based early warning indicators have likewise been used to argue that the circulation is approaching a tipping point (van Westen et al., 2024, 2025). Nevertheless, the interpretation of these early warning signals has been challenged in a recent study (Zimmerman et al., 2025).

A companion analysis of the same CMIP6 large ensemble archive used below, by some of the present authors, further divides this variability into three successive physical regimes over 1850–2100 and identifies profound changes in the AMOC internal variability over the current century (Coquereau et al., 2026). Coupled climate models broadly agree that the circulation weakens during the twenty-first century (Weijer et al., 2020), with a magnitude tied to the pathways along which the overturning is organised (Baker et al., 2023), and observational constraints on these projections point to a weakening of about 50 % by 2100 (Portmann et al., 2026). They disagree sharply, however, on what follows: some models retain an overturning circulation, weakened but present, even under extreme forcing (Baker et al., 2025), whereas others show a shutdown after 2100 following a collapse of deep mixing (Drijfhout et al., 2025).

We take this body of oceanographic and statistical work as our physical starting point, but we ask a narrower and more strictly mathematical question of the same simulations, and we ask it of their future rather than their past. Setting aside any particular physical mechanism or scalar index, does the high dimensional state of the simulated circulation move onto a qualitatively distinct dynamical regime under continued forcing, and does the answer depend on the emission pathway? The historical segment enters the analysis mainly as a reference against which the projections are read: over that period the simulated circulation stays on a single regime (Sect. 4.2), so the transitions we characterise are ones the model produces after the 2015 branch point. We make no claim here about whether the observed circulation has already changed regime, and we return to physical interpretation only in the discussion (Sect. 5).

Evidence bearing on such transitions, whether observed or simulated, rests almost entirely on scalar or low dimensional proxies of the AMOC: sea surface temperature fingerprints, subpolar gyre indices, or basin averaged transport time series. These are analysed with indicators of critical slowing down, chiefly rising variance and rising lag-1 autocorrelation (Boers, 2021). Such indicators are attractive because they need little more than a single time series. But they are built on a linearisation around a slowly drifting equilibrium, and they are therefore blind to genuinely nonlinear or multivariate reorganisations of the circulation, which may leave little trace in the one scalar chosen for analysis.

https://doi.org/10.5194/egusphere-2026-6552
Preprint. Discussion started: 13 November 2026
© Author(s) 2026. CC BY 4.0 License.

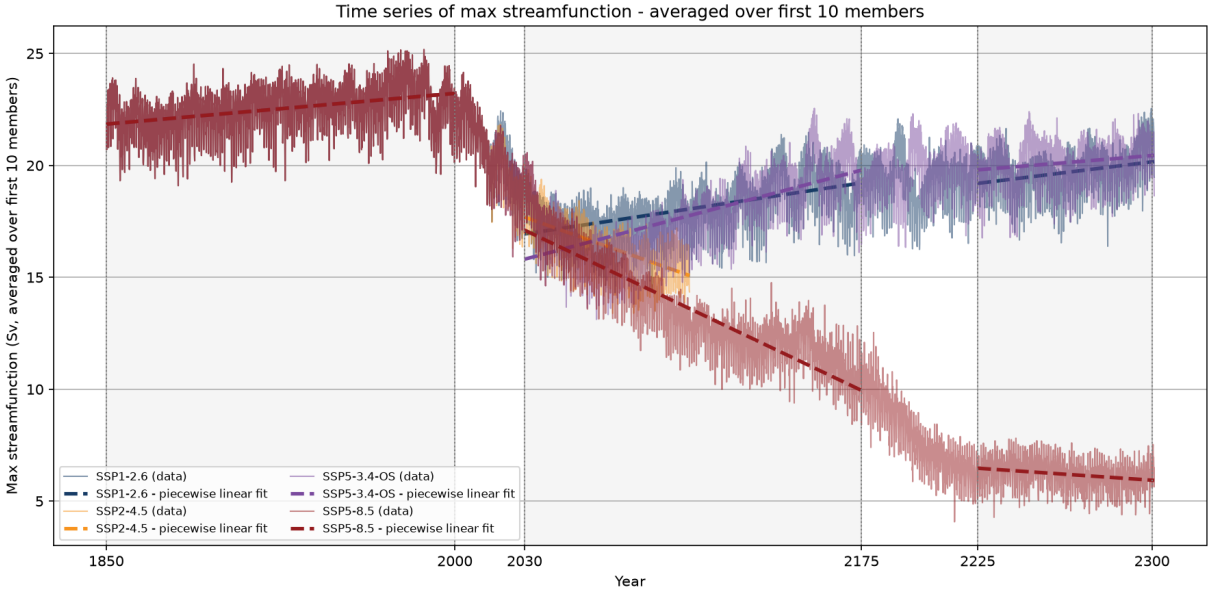


Figure 1. Maximum overturning current $\psi_{\max}(t)$, the largest value of the AMOC streamfunction over the core of the overturning cell, 35–55°N and 500–1500 m (Sect. 3.3), for the historical run continued under SSP1-2.6 (dark blue), SSP2-4.5 (orange), SSP5-3.4-OS (purple) and SSP5-8.5 (dark red); SSP2-4.5 is available only to 2100, the three others extend to 2300. Each series is averaged over the first ten ensemble members.

The simulations analysed in this paper illustrate this limitation (Fig. 1). Their conventional scalar index, the maximum of the overturning streamfunction, weakens after 2015 under all four emission scenarios considered here. Under the highest one it keeps declining until the end of the simulations, and under the intermediate one it is still declining when the simulations end in 2100; under the lowest one, and under the overshoot pathway once its CO_2 concentration declines, it recovers partially. Seen through this index alone, the scenarios differ in degree rather than in kind. What it cannot tell us is whether these are weakenings of the same circulation, or whether, under some scenarios, the circulation has changed the way it operates.

A complementary strategy has been developed mainly in the dynamical systems and statistical mechanics literature on weather and climate. It treats the full field, rather than a single index, as the state of a high dimensional dynamical system, and it describes directly the geometry of the attractor, or attractors, that this state visits. Its main tool is the *local dimension* $d(\zeta)$: an estimate of how many degrees of freedom are effectively active in the neighbourhood of a reference state ζ. This quantity is conventionally computed through Extreme Value Theory (Freitas et al., 2010; Lucarini et al., 2016; Faranda et al., 2017; Faranda and Vaienti, 2018; Caby et al., 2021; Faranda et al., 2024). The conventional estimator has two drawbacks for our purposes. It carries a known bias driven by the local density of points (Platzer and Chapron, 2025), and it requires assumptions, among them regular variation of the invariant measure and stationarity (del Amo et al., 2025), that do not hold for the forced,

https://doi.org/10.5194/egusphere-2026-6552
Preprint. Discussion started: 13 November 2026
© Author(s) 2026. CC BY 4.0 License.

non-stationary trajectories analysed here. We therefore use an alternative from the manifold learning literature, with lower bias and lighter assumptions: the Expected Simplex Skewness (ESS) estimator of Johnsson et al. (2015), detailed in Sect. 3.2.

Our other diagnostic, and the one from which our analysis starts, is a low dimensional embedding of the monthly circulation state, obtained with Uniform Manifold Approximation and Projection (UMAP; McInnes et al., 2018). It lets us see whether the trajectory stays within a single region of state space or migrates between distinct regions over time. Embeddings of this kind can produce apparent structure that reflects the projection algorithm rather than genuine structure in the data (Chari and Pachter, 2023; Kobak and Linderman, 2021). We therefore treat UMAP as an exploratory tool that generates hypotheses, not as evidence in its own right, and we corroborate whatever it suggests with the ESS local dimension, computed independently in the full, un-projected phase space (Sect. 3). The two diagnostics are built from unrelated mathematical machinery, yet they answer the same question. When they agree, the result is far harder to explain away as an artefact of either method than a claim resting on either one alone.

In this paper we apply ESS and UMAP together to the AMOC as simulated by the ACCESS Earth system model contributions to CMIP6 (Eyring et al., 2016; Ziehn et al., 2020), whose ocean component is shared with the physical model ACCESS-CM2 (Bi et al., 2020). We use the historical experiment and four scenarios of Shared Socioeconomic Pathways (O'Neill et al., 2016): the low, intermediate and high forcing pathways SSP1-2.6, SSP2-4.5 and SSP5-8.5, and the overshoot pathway SSP5-3.4-OS, which follows SSP5-8.5 until 2040 and then undergoes rapid mitigation, so that the CO_2 concentration peaks and declines. All reach 2300 except SSP2-4.5, which ends in 2100. Our question is simple. Viewed as a high dimensional dynamical system rather than through a single scalar index, does the AMOC show evidence of a qualitative change of regime, and if so, does that change depend on the scenario? The overshoot pathway adds a second question: can a circulation pushed along the high forcing trajectory for several decades still return to its original regime once the forcing is reversed? We find that the response depends on the scenario, and that the overshoot is reversible in this model, as detailed in Sect. 4. Section 2 describes the CMIP6 ACCESS data and the construction of the phase space. Section 3 details the UMAP embedding and the ESS estimator. Section 4 presents the UMAP attractor geometry and its relationship to local dimension, phase space velocity and maximum overturning current, followed by the local dimension and velocity time series across scenarios and their statistics over three successive periods (Table 2), and finally by the relation of the displacement of the state and of the maximum overturning current to the CO_2 forcing.

2 Data

We use monthly output from the Australian Community Climate and Earth System Simulator (ACCESS) contribution to CMIP6 (ACCESS-ESM1.5), obtained from the public archive via the Earth System Grid Federation (ESGF). We chose ACCESS for two reasons: it provides a comparatively large number of initial condition ensemble members, and it runs to 2300. Few other CMIP6 models offer both. We analyse the CMIP6 `historical` experiment (1850–2015) and its continuation under four Scenarios of Shared Socioeconomic Pathways (O'Neill et al., 2016): SSP1-2.6 (low forcing), SSP2-4.5 (intermediate forcing), SSP5-8.5 (high forcing), and SSP5-3.4-OS (overshoot). SSP5-3.4-OS is identical to SSP5-8.5 until 2040, after which

https://doi.org/10.5194/egusphere-2026-6552
Preprint. Discussion started: 13 November 2026
© Author(s) 2026. CC BY 4.0 License.

its emissions fall steeply, so that the CO_2 concentration peaks and then declines; it thus probes whether the circulation recovers from a temporary exposure to the high forcing trajectory. SSP1-2.6, SSP5-8.5 and SSP5-3.4-OS run to 2300, and SSP2-4.5 to 2100 (Table 1).

Table 1. CMIP6 ACCESS-ESM1.5 experiments used in this study.

Experiment	Forcing pathway	Period	Role
`historical`	Observed historical forcing	1850–2014	Common reference trajectory
`ssp126`	SSP1-2.6 (low forcing)	2015–2300	Low emission continuation
`ssp245`	SSP2-4.5 (intermediate forcing)	2015–2100	Intermediate continuation
`ssp534-over`	SSP5-3.4-OS (overshoot)	2041–2300	Overshoot continuation[a]
`ssp585`	SSP5-8.5 (high forcing)	2015–2300	High emission continuation

[a] SSP5-3.4-OS follows SSP5-8.5 until 2040; for each member, 2015–2040 is therefore taken from the same member's `ssp585` run, and the `ssp534-over` output from 2041 onward.

The four scenarios are run in concentration driven mode: the atmospheric CO_2 mole fraction is prescribed from the input4MIPs dataset of Meinshausen et al. (2020), whose global mean we show in Fig. 2. We use this prescribed concentration below as the measure of the forcing each scenario applies, both to colour the UMAP embedding (Fig. 4) and to relate the timing of the AMOC response to that of the forcing.

The variable we analyse is the CMIP6 `msftmz` field, which we call simply the streamfunction below. We keep the monthly fields on a regular grid of 30 latitude points spanning 0–70°N and 18 depth levels spanning 0–2000 m. Flattening the two spatial coordinates into a single state vector gives, for each calendar month t, a point

$$\mathbf{x}(t) \in \mathbb{R}^D, \qquad D = 30 \times 18 = 540, \tag{1}$$

so the monthly sequence $\{\mathbf{x}(t)\}$ is a trajectory in a 540-dimensional phase space. We normalise these state vectors before the geometric analyses, so that the UMAP embedding of Sect. 3.1 and the local dimension of Sect. 3.2 are computed on the normalised states; the phase space velocity and the maximum overturning current of Sect. 3.3 are reported in physical units instead, in Sverdrups (Sv). In either case we work with the state itself, not with anomalies relative to a climatology.

For each scenario we analyse the first ten initial condition ensemble members. Ten is the number of members extended beyond 2100 under SSP1-2.6 and SSP5-8.5, and we use the same ten for SSP2-4.5 and SSP5-3.4-OS so that every diagnostic below is computed with identical parameters across scenarios: the local dimension in particular depends on the size of the catalogue it is estimated from (Sect. 3.2), so a scenario analysed with more members would not be directly comparable with one analysed with fewer. Each member is one continuous monthly record: the historical segment, followed by that scenario's continuation (for SSP5-3.4-OS, the same member's SSP5-8.5 run over 2015–2040, then the overshoot run; Table 1). Under SSP1-2.6, SSP5-8.5 and SSP5-3.4-OS a member therefore spans 1850–2300, which is 451 years and

$$T = 451 \times 12 = 5412 \tag{2}$$

https://doi.org/10.5194/egusphere-2026-6552
Preprint. Discussion started: 13 November 2026
© Author(s) 2026. CC BY 4.0 License.

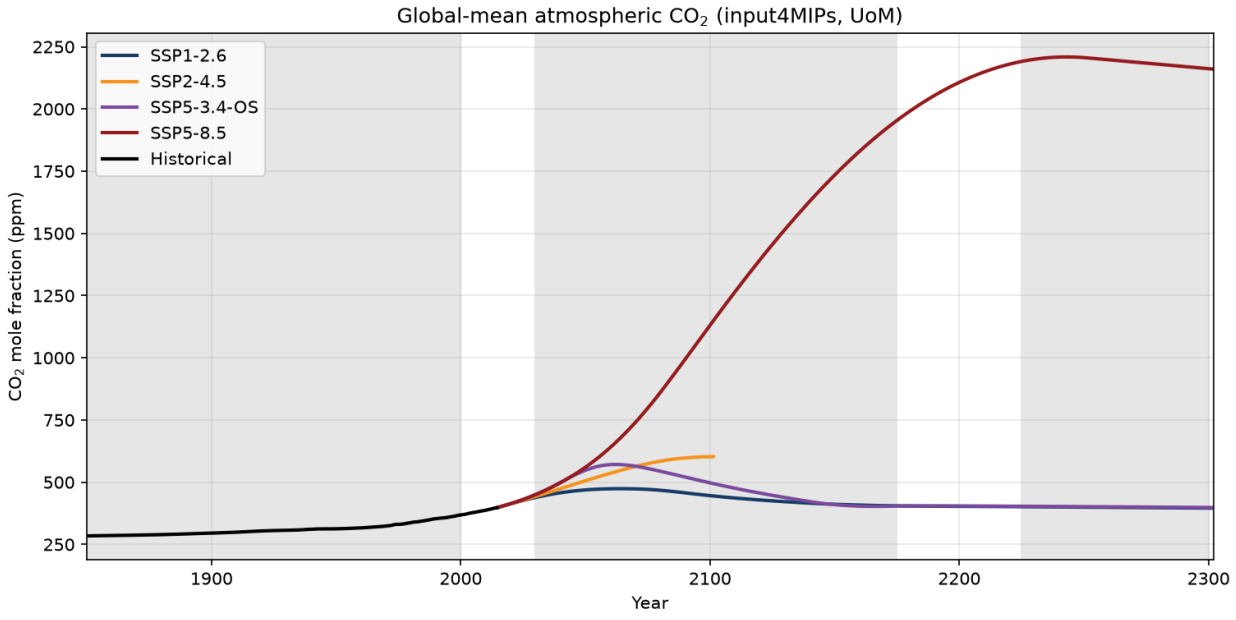


Figure 2. Global mean atmospheric CO_2 mole fraction (ppm) prescribed to ACCESS-ESM1.5 in the historical experiment (black) and under SSP1-2.6, SSP2-4.5, SSP5-3.4-OS and SSP5-8.5 (input4MIPs, Meinshausen et al., 2020), over the period of the simulations. Grey bands mark the three periods of Table 2.

monthly states, so the ten members together give $10 \times T = 54{,}120$ states per scenario. SSP2-4.5 stops in 2100 and is shorter: $T = 251 \times 12 = 3012$ states per member, and 30,120 in all. We use these same states throughout. They are pooled, across members and across scenarios alike, to fit the single UMAP embedding of Sect. 3.1. Each state enters that fit once: the historical segment common to all scenarios is entered once rather than once per scenario, and so is the 2015–2040 segment that SSP5-3.4-OS shares with SSP5-8.5 (Sect. 3.1). The fit therefore uses the $1980 \times 10 = 19{,}800$ historical states together with the 110,160 distinct states of the four continuations (34,320 each for SSP1-2.6 and SSP5-8.5, 10,320 for SSP2-4.5 and 31,200 for the part of SSP5-3.4-OS after 2040), 129,960 in all. The same states form the neighbour catalogue from which the local dimension of Sect. 3.2 is estimated, scenario by scenario; and they are the states over which the diagnostics of Sects. 3.2–3.3 are computed member by member and then averaged.

3 Methods

3.1 UMAP embedding

To get a first, visual sense of whether the circulation moves between distinct regimes, we reduce each monthly, 540-dimensional state to just two coordinates using Uniform Manifold Approximation and Projection (UMAP; McInnes et al., 2018), a widely used dimensionality reduction technique. UMAP works out which monthly states resemble which others in the original high

https://doi.org/10.5194/egusphere-2026-6552
Preprint. Discussion started: 13 November 2026
© Author(s) 2026. CC BY 4.0 License.

dimensional space. It then places the points in two dimensions so that similar states end up close together and dissimilar states end up far apart. The result is a scatter plot in which structure spread across 540 dimensions can be inspected directly, and which we colour by whichever quantity is of interest at each state: the year it belongs to, its ESS local dimension, its phase space velocity or its maximum overturning current (Sects. 3.2–3.3). Its main advantage here is that it tends to preserve both the fine relationships between neighbouring states and the broad overall layout of the data. If the circulation really does occupy two distinct regions of state space at different times, this should therefore appear as two separated regions in the plot rather than being blurred into one. That makes UMAP well suited to showing the region or regions, the "attractors", that the circulation visits, and to revealing any transition between them. Methods of this kind can, however, sometimes produce clusters or gaps that come from the algorithm rather than from the data (Chari and Pachter, 2023; Kobak and Linderman, 2021). Any transition the UMAP picture suggests therefore has to be confirmed independently before we can treat it as a real dynamical feature. We use the local dimension of the attractor for that confirmation, and turn to it next (Sect. 3.2).

Every UMAP embedding shown in Sect. 4.1 from Fig. 3 onward comes from a single fit, performed once on the monthly normalised states of all ten ensemble members of all four scenarios simultaneously (Sect. 2). There is therefore one embedding in this paper, not four: the panels of Figs. 3–7 are views of that same embedding, each restricted to the states of one scenario, and they share one set of axes on which the value of each diagnostic at every point can be read directly and compared across scenarios. Fitting the four scenarios together has one consequence we rely on throughout. The 1850–2014 historical segment is common to them, and enters the fit once rather than once per scenario; likewise, the 2015–2040 segment of SSP5-3.4-OS, identical to that of SSP5-8.5, enters once, so that no state is duplicated. The pre-2015 cloud is therefore not merely identical in appearance from panel to panel, it is the same set of embedded points, and any difference between panels is a difference between the post-2015 continuations rather than between separately optimised layouts. Pooling the ten members is justified by their construction: they are initial condition replicas of the same model under the same forcing, so they sample the same attractor, and pooling them buys a denser sampling of it than any single trajectory provides. The local dimension and phase space velocity series are built differently (Sects. 3.2–3.3). They do not enter a single fit; each is computed member by member, over those same ten members, and then averaged.

3.2 Local dimension as a corroborating diagnostic

We use the local dimension for two things. First, to characterise the attractor on which the circulation evolves: how many degrees of freedom it engages, and whether that number is stable over time. Second, to detect transitions between attractors, that is, changes in the dynamics themselves rather than in the strength of the circulation. It is the diagnostic against which we test the UMAP picture throughout, and it can serve that purpose because it is computed in the un-projected 540-dimensional phase space and shares none of the embedding's machinery. This section defines the quantity, explains which estimator we use for it and why, and sets out how we compute it.

Take a set of states $\{\mathbf{x}(t)\}_{t=1}^{T}$ that sample an attractor $\mathcal{A}$. The *local dimension* of $\mathcal{A}$ at a reference state ζ says how many degrees of freedom are effectively active in the immediate neighbourhood of ζ. It is a property of the attractor, or equivalently of the manifold on which the data lie, sampled at ζ, and not of the particular trajectory used to sample it. Two literatures

https://doi.org/10.5194/egusphere-2026-6552
Preprint. Discussion started: 13 November 2026
© Author(s) 2026. CC BY 4.0 License.

make the idea precise in genuinely different ways. The classical dynamical systems version, which we call the *measure based* notion, assumes an invariant measure μ on $\mathcal{A}$ and defines $d(\zeta)$ as the scaling exponent of $\mu(B(\zeta,r))$, the measure of a ball of radius r around ζ, as $r \to 0$; intuitively, it asks how the number of points inside a small ball around ζ changes as the ball shrinks. This is what EVT-based estimators, including MLE, target. ESS targets a *manifold based* notion instead, which refers neither to an invariant measure nor to a fixed attractor: it assumes only that the data lie on, or are scattered with noise around, a d-dimensional manifold near ζ, and estimates the dimension of that manifold from the local geometry of the neighbours themselves, for example from how the volumes of simplices spanned by nearby points scale.

Strictly, these are different mathematical objects, and no formal equivalence between them is guaranteed. The configurations that drive them apart, however, are pathological ones: measures whose scaling exponent differs from the dimension of the set supporting them, strongly singular or non-rectifiable invariant sets, neighbourhoods in which the measure concentrates anisotropically at every scale. Systems of that kind are constructed, or arise in low dimensional idealised maps; they are not what a dissipative, smoothly forced geophysical flow produces, and they are further smoothed away by finite spatial resolution, monthly averaging and the model's own numerical dissipation. For a system of the kind analysed here, then, the data near any reference state lie close to a well behaved manifold, the invariant measure varies regularly along it, and the two notions count the same active directions. We therefore treat the distinction as technical rather than practical in this application: it matters for which hypotheses an estimator must assume, which is why we take it seriously in choosing one below, but not for what the resulting number means. Under either notion, a qualitative reorganisation of the dynamics, such as the emergence of a new set of dominant balances in the circulation, should leave a signature in $d(\zeta)$ as ζ is taken along the trajectory, even if it is not obvious in any single scalar projection of the field. This is what makes the quantity usable for the second purpose above.

Intrinsic dimension estimation is a substantial field in its own right within the manifold learning community, which has produced a large number of estimators together with benchmark studies comparing them (Rozza et al., 2012; Campadelli et al., 2015). In the geophysical literature, by contrast, local dimension is estimated almost exclusively with an EVT-based approach applied to the statistics of close returns to a reference state (Freitas et al., 2010; Faranda et al., 2017; Lucarini et al., 2016; Caby et al., 2021; Faranda et al., 2024). This is the same estimator that the manifold learning literature calls the Maximum Likelihood Estimator (MLE) of Levina and Bickel (2004), the two communities having developed and named it largely independently. Its limitations are documented in those benchmarks: a substantial bias driven by density effects (Platzer and Chapron, 2025), a systematic underestimation of the local dimension, a comparatively strong sensitivity to the curse of dimensionality, and, because it targets the measure based notion, a requirement of regular variation of the invariant measure (del Amo et al., 2025) and indeed of a stationary measure at all. Those last hypotheses sit poorly with the non-stationary trajectories analysed here.

We therefore select an estimator from the wider set rather than defaulting to the geophysical convention, and we use the Expected Simplex Skewness (ESS) estimator of Johnsson et al. (2015). Two properties decided the choice. First, it retains its accuracy in high dimension, where most estimators degrade sharply; with $D = 540$ ambient coordinates and local dimensions of order twenty, this is the binding constraint on our analysis. Second, its bias is considerably lower than that of MLE, which matters because our conclusions rest on differences of a few dimension units between periods and scenarios rather than on

https://doi.org/10.5194/egusphere-2026-6552
Preprint. Discussion started: 13 November 2026
© Author(s) 2026. CC BY 4.0 License.

the absolute value of $\hat{d}$. That ESS targets the manifold based notion, and so requires neither a stationary measure nor regular variation of it, is a further advantage given the forced trajectories analysed here.

ESS does not fit a tail distribution to a single scalar observable. It exploits instead the concentration of measure phenomenon in the geometry of local neighbourhoods. For a reference point ζ_i and its k nearest neighbours, assumed to form a patch of the underlying manifold with low curvature and low noise, simplices are formed from the neighbour difference vectors and a normalised skewness statistic of their volumes is computed. In expectation this statistic varies monotonically with the intrinsic dimension of the local patch, so comparing the observed value against Monte Carlo reference curves, computed for points drawn uniformly from hyperballs of known dimension $d = 1, 2, \ldots, D_{\max}$, gives a low bias estimate $\hat{d}(\zeta_i)$ by inversion. We set $k = 50$ throughout.

For each calendar month t and each of the ten ensemble members $m = 1, \ldots, 10$ of a run, we compute $\hat{d}_m(t) = \hat{d}(\mathbf{x}_m(t))$ from the k nearest neighbours of $\mathbf{x}_m(t)$, measured by Euclidean distance in the normalised state space of Sect. 2. Neighbours are drawn from the states of all ten members of that run, not from member m's own trajectory alone. Pooling the members gives a denser sampling of the phase space, and so more analogues for each reference state, which matters for an estimator whose bias grows as the neighbourhood becomes sparse. The series reported below, $\hat{d}(t)$, is the average of $\hat{d}_m(t)$ over the ten members, computed separately for the historical run and each of the four scenario continuations, at native monthly resolution.

3.3 Phase space velocity and maximum overturning current

To connect the geometry of the UMAP embedding (Sect. 3.1) more directly to the underlying dynamics, we compute two further diagnostics at each monthly state $\mathbf{x}(t)$. The first is the *phase space velocity*, in the form introduced by Caby et al. (2026),

$$v(t) = \frac{\|\mathbf{x}(t+1) - \mathbf{x}(t)\|}{\Delta t}, \qquad \Delta t = 1 \text{ month}. \tag{3}$$

It measures how fast the trajectory moves through the full 540-dimensional phase space. Because the state vector carries the streamfunction in Sverdrups, $v(t)$ is expressed in Sv per month, and it is directly comparable between members and between scenarios without further rescaling. $v(t)$ is best read as a measure of how active the dynamics are at the current state, rather than as a marker of which regime the state belongs to. Near a stable, strongly attracting configuration, where the state is pulled back toward the same neighbourhood from one month to the next, $v(t)$ should be low. Where the dynamics are less constrained, and the state can travel further in a month, it should be higher. As with the local dimension (Sect. 3.2), each member's $v(t)$ is computed along its own trajectory, and the series reported in Sect. 4.3 is the average over the ten members. We use $v(t)$ both to colour the UMAP embedding (Fig. 6) and, in Sect. 4.3, as a phase space time series analogous to the ESS local dimension of Sect. 4.2.

The second diagnostic is the *maximum overturning current*,

$$\psi_{\max}(t) = \max_{\substack{35^\circ\mathrm{N} \le \text{lat} \le 55^\circ\mathrm{N} \\ 500\,\mathrm{m} \le \text{depth} \le 1500\,\mathrm{m}}} \mathbf{x}(t), \tag{4}$$

https://doi.org/10.5194/egusphere-2026-6552
Preprint. Discussion started: 13 November 2026
© Author(s) 2026. CC BY 4.0 License.

the largest value of the streamfunction field at time t over the core of the overturning cell. The maximum is restricted to this subdomain, drawn on Fig. 8, so that it measures the overturning cell itself: over the full domain it can instead be set by the subpolar gyre at high latitudes, or by the wind driven circulation of the upper few hundred metres, neither of which belongs to the overturning cell. This is the conventional scalar AMOC strength index used throughout the literature discussed in Sect. 1, and it gives a direct link between our high dimensional diagnostics and the scalar proxies they are usually compared against. To some extent it is a measure of the solid rotation within the latitude-depth plane induced by the flow (ignoring deformation and spatial variation of the rotation). We report it in Sverdrups, converting the native mass transport of the CMIP6 `msftmz` field at the conventional rate of 10^9 kg s^{-1} per Sverdrup, so that it can be read directly against the values quoted in that literature: the historical mean in Table 2 is 22.53 Sv.

Finally, to follow how far the circulation moves from its initial state within the UMAP embedding, we compute a *sliding barycentre* of the embedded states. For each month t, $\mathbf{b}(t)$ is the mean of the two dimensional UMAP coordinates of all states, of all ten members, whose date lies within a ten year window centred on t, $[t-5\,\mathrm{yr}, t+5\,\mathrm{yr}]$; the window is truncated at the ends of the record. We then define the *barycentre distance*

$$D(t) = \|\mathbf{b}(t) - \mathbf{b}(t_0)\|, \tag{5}$$

the Euclidean distance in the embedding between the barycentre at time t and the first barycentre of the record, $\mathbf{b}(t_0)$, which averages the states of 1850–1855. Averaging over ten years and ten members removes most of the month to month and inter-member variability, so that $D(t)$ follows the slow drift of the cloud of states rather than the position of any single one. The same quantity computed for each member separately, against the same reference $\mathbf{b}(t_0)$, shows the spread around it. Because $D(t)$ is measured in the embedding, it inherits the caveats of Sect. 3.1: UMAP preserves the ordering of large distances better than their magnitude, so we use $D(t)$ to compare states and scenarios on the common axes of the single joint fit, not as a metric distance in the original phase space.

4 Results

4.1 UMAP embedding of the AMOC state

4.1.1 Regime geometry across scenarios

We fit a single embedding to the ten members of the four scenarios together (Sect. 3.1). Figure 3 shows it, coloured by year, restricted in turn to the states of each scenario.

In all four panels the pre-2015 historical states occupy a compact region of the embedding, which we call Regime A. That region is not merely similar between panels but the same one: the historical record is common to the four scenarios and the embedding is fitted to them jointly (Sect. 3.1), so those states carry the same coordinates wherever they appear. What the four panels show is therefore one cloud of historical states together with four different continuations out of it, and the panels can be laid over one another and read against a common origin. The comparisons drawn below rest on this. Where the post-2015 states

https://doi.org/10.5194/egusphere-2026-6552
Preprint. Discussion started: 13 November 2026
© Author(s) 2026. CC BY 4.0 License.

of one scenario lie relative to Regime A can be compared directly with where those of another lie, because both are expressed on the same axes and measured from the same starting cloud. The corroboration of this geometry does not, in any case, come from the embedding: the local dimension and the phase space velocity (Sects. 4.2–4.3) are computed in the un-projected 540-dimensional phase space, and the local dimension in particular is estimated scenario by scenario, from a neighbour catalogue containing only that scenario's own states (Sect. 3.2), so it shares nothing with the joint fit used here.

The four scenarios then behave differently. Under SSP1-2.6 (panel a), the post-2015 trajectory is displaced away from Regime A while the CO_2 concentration is still rising, but once the concentration has peaked (around 2060, Fig. 2) and begins to decline it returns, so that the late states (2100–2300) overlap the pre-2015 cloud again rather than settling into a separate, persistent region. This is an excursion under forcing that is undone once the forcing itself is undone, not a lasting reorganisation of the attractor. Hence this attractor modification can be considered as "reversible", in the sense that the initial attractor is retrieved as the anthropogenic forcing recovers low values. Under SSP2-4.5 (panel b), the trajectory drifts substantially further, toward a second, distinguishable region that we call Regime B, but only some of the late states reach it and the rest stay closer to Regime A. This is an incomplete, intermediate version of the SSP5-8.5 transition, and, whereas SSP1-2.6 is already heading back toward Regime A by 2100, it shows no sign of doing so by that date, the last year available for this scenario. Under SSP5-3.4-OS (panel c), the trajectory first follows the SSP5-8.5 continuation, as it must, the forcing being identical until 2040: it leaves Regime A along the same pathway, and travels further along it than under SSP1-2.6. Once the concentration peaks and declines, however, it turns back, and the late states (2100–2300) overlap the pre-2015 cloud again, so that the late picture is very close to that of SSP1-2.6. The excursion is larger than under SSP1-2.6, but it is reversed in the same way: the overshoot is "reversible" in the same sense. Under SSP5-8.5 (panel d), the trajectory traces a visibly narrow path from Regime A to a distinct Regime B: rather than spreading out as it moves, the point cloud pinches inward during 2015–2200 and widens again once Regime B is reached. By 2200–2300 the great majority of states lie in Regime B, clearly separated from the pre-2015 cloud, with no sign of a return. The concentration under this scenario keeps rising until about 2250 and only then levels off (Fig. 2); over the remaining 2250–2300 period of stable forcing, the trajectory shows no sign of returning toward Regime A, and in this sense the change is "non-reversible" within the simulated period. The corridor is not uniformly populated: it contains visible voids, regions the embedded trajectory appears to route around rather than through. We note this without pressing it. Such gaps are among the features that embeddings of this kind can manufacture (Chari and Pachter, 2023; Kobak and Linderman, 2021), and at these sampling densities they are also what one would expect of any projection of a high dimensional cloud; but they would equally be consistent with the transition following preferred routes through state space, with some intermediate configurations rarely or never realised. Distinguishing the two would require evidence in the un-projected phase space that we do not attempt here.

Read side by side, the four panels look less like four different responses than like one response carried to different distances. The pathway out of Regime A is common to the scenarios: the trajectory leaves the historical cloud in the same direction in all four, and what distinguishes them is how fast it travels along that pathway and how far it has gone by the time the concentration stops rising (around 2060 under SSP1-2.6 and SSP5-3.4-OS, around 2250 under SSP5-8.5; Fig. 2). The pace increases with the forcing. Under SSP1-2.6 the state is still close enough to Regime A when the concentration peaks and starts to decline that

https://doi.org/10.5194/egusphere-2026-6552
Preprint. Discussion started: 13 November 2026
© Author(s) 2026. CC BY 4.0 License.

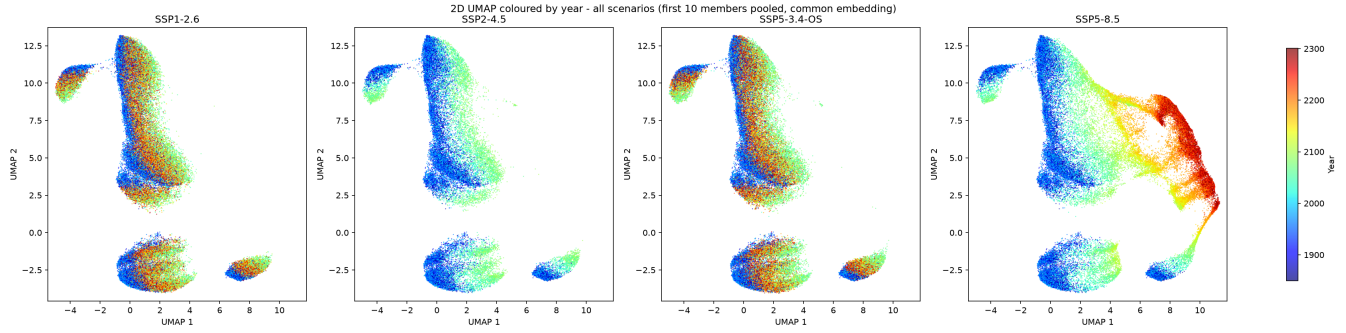


Figure 3. The multi-member, multi-scenario two dimensional UMAP embedding introduced in Sect. 3.1, coloured here by year, for (a) SSP1-2.6, (b) SSP2-4.5, (c) SSP5-3.4-OS and (d) SSP5-8.5, from left to right; SSP2-4.5 ends in 2100. The four panels are one embedding, fitted to the ten members of the four scenarios together and here restricted to the states of each scenario in turn; the axes and the pre-2015 cloud are consequently identical between them.

the excursion is reversed and the historical cloud is recovered; in the language of dynamical systems, the trajectory has never left the basin of attraction it started in. Under SSP5-8.5 it has travelled far enough, and through enough of the corridor, that the levelling off of the concentration after 2250 does not bring it back, at least by 2300: the circulation stays in Regime B, which is what one expects of a tipping point rather than of a forced displacement. SSP5-3.4-OS sits between the two and makes this reading testable. Its trajectory is pushed along the SSP5-8.5 pathway until the forcing is reversed, and so goes further from Regime A than SSP1-2.6 does; yet it is recovered in the same way. At the time its forcing peaks, it has therefore not yet left the basin of attraction of Regime A either. Whatever point of the pathway marks the boundary of that basin, it lies beyond the furthest state reached under SSP5-3.4-OS, and before the states SSP5-8.5 had reached when its own concentration levelled off. SSP2-4.5 cannot be followed past 2100, but by then it lies on the same pathway well beyond the point at which SSP1-2.6 turned back, and, with a concentration still rising, shows no sign of returning. Together with the local dimension (Sect. 4.2.2), this is why we expect it to be heading for Regime B rather than about to be reversed.

Colouring the same embedding by the prescribed CO_2 concentration rather than by year (Fig. 4) puts this reading to a direct test. If the position of the state along the common pathway were set by the level of forcing alone, a given concentration would map onto the same region of the embedding in all four panels. Broadly, the figure is consistent with this reading: in every scenario the state lies further from Regime A the higher the concentration, and under SSP1-2.6 and SSP5-3.4-OS it returns toward Regime A as the concentration declines. A finer comparison is limited by the colour scale, however. Being common to the four panels, it must span the full range of SSP5-8.5, whose concentration exceeds 2000 ppm, whereas those of the other scenarios remain within a few hundred ppm of present day values; their states therefore occupy a narrow band of colours, and moderate differences in concentration between them cannot be resolved by eye. This is the case in particular for the question of whether SSP5-8.5 reaches a given point of the pathway at a higher concentration than SSP2-4.5, which would indicate a lag of the circulation behind its forcing. We return to the relation between the state and its forcing, quantitatively, in Sect. 4.4, once

https://doi.org/10.5194/egusphere-2026-6552
Preprint. Discussion started: 13 November 2026
© Author(s) 2026. CC BY 4.0 License.

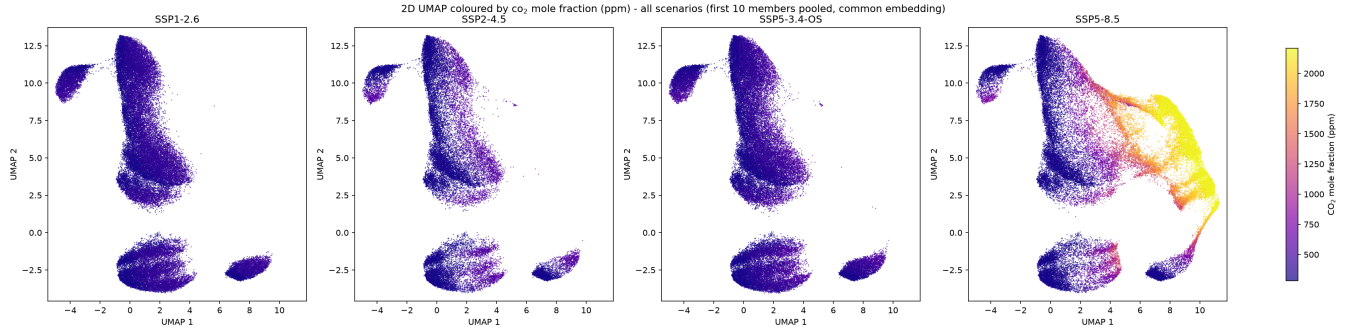


Figure 4. Multi-member UMAP embedding as Fig. 3, coloured here by the global mean atmospheric CO_2 concentration (ppm) prescribed at the date of each state (Fig. 2). The colour scale is common to the four panels.

the other diagnostics have been established; there the displacement of the state is plotted against the concentration itself, on a logarithmic axis that resolves the lower concentrations.

4.1.2 Relating the embedding to local dimension, velocity, and streamfunction strength

Taken together, this geometry suggests a graded, scenario dependent AMOC response rather than a single transition that is simply present or absent: a lasting migration to a distinct attractor under SSP5-8.5, a migration under way but unfinished when the record ends under SSP2-4.5, and transient excursions that reverse once the forcing peaks and declines, under SSP1-2.6 and, after travelling further along the same pathway, under SSP5-3.4-OS. Because nonlinear embeddings such as UMAP can produce clusters, gaps or corridors that come from the algorithm rather than the data (Sect. 3.1), we do not take this at face value. We first relate it, point for point, to the diagnostics of Sect. 3.3: the ESS local dimension (Fig. 5), the phase space velocity (Fig. 6) and the maximum overturning current (Fig. 7). We then turn, in Sect. 4.2, to a fully independent confirmation computed directly in the un-projected 540-dimensional phase space.

Relating the embedding with the ESS local dimension $\hat{d}(t)$ (Fig. 5) shows the narrow transition corridor, previously seen under SSP5-8.5 (Fig. 3d), coinciding, point for point, with a region of markedly lower $\hat{d}(t)$. The same correspondence holds under SSP2-4.5, whose post-2015 states reach into the corridor. Under SSP1-2.6 and SSP5-3.4-OS, whose trajectories do not enter the corridor, any reduction of $\hat{d}(t)$ is transient and much weaker, consistent with their period means (Table 2).

Relating the embedding with the phase space velocity $v(t)$ instead (Fig. 6), there is no increase within the corridor itself. Instead $v(t)$ decreases steadily along the pathway from Regime A to Regime B, with a slope that is steeper for the higher emission scenarios.

Finally, we relate the embedding with the maximum overturning current $\psi_{\max}(t)$ (Fig. 7), the conventional scalar AMOC strength index (Sect. 3.3). Wherever Regime B is reached it is systematically weaker than Regime A, and the transition corridor spans intermediate values between the two. This is consistent with the scalar index evidence for AMOC weakening discussed in Sect. 1 (Rahmstorf et al., 2015; Weijer et al., 2020; Boers, 2021; Ditlevsen and Ditlevsen, 2023; Portmann et al., 2026).

https://doi.org/10.5194/egusphere-2026-6552
Preprint. Discussion started: 13 November 2026
© Author(s) 2026. CC BY 4.0 License.

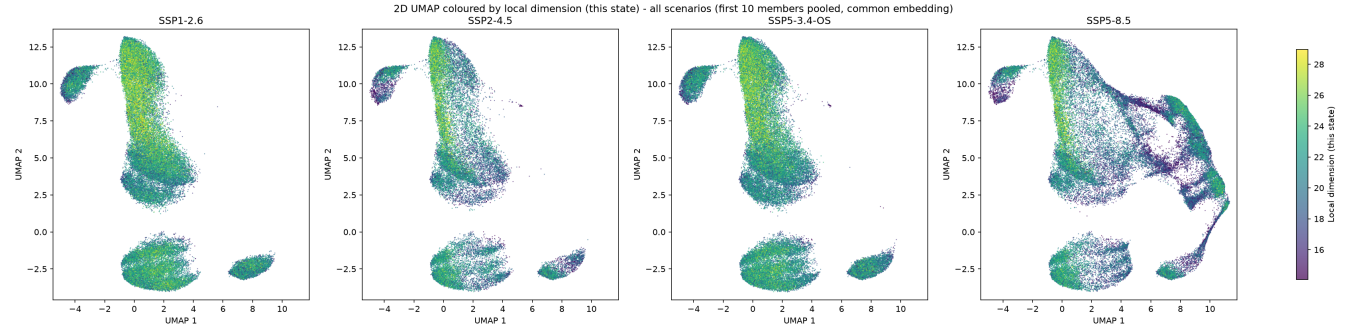


Figure 5. Multi-member UMAP embedding as Fig. 3, coloured here by ESS local dimension $\hat{d}(t)$.

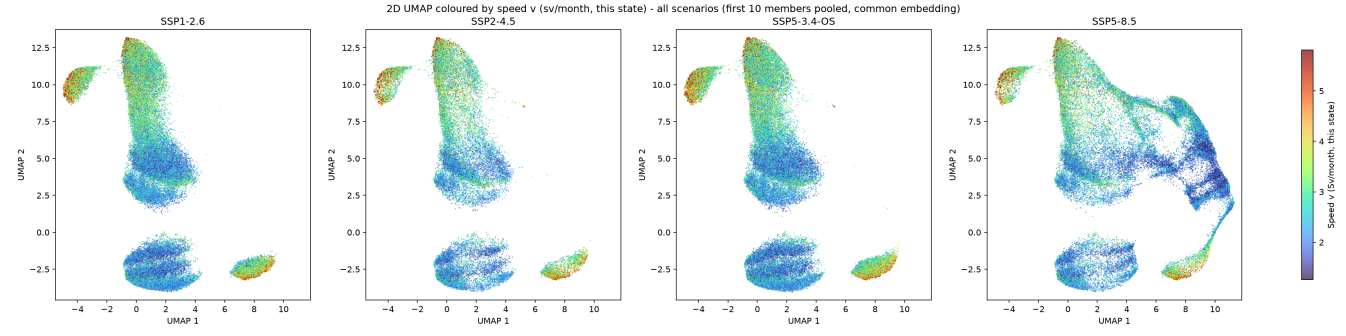


Figure 6. Multi-member UMAP embedding as Fig. 3, coloured here by phase space velocity $v(t)$ (Sect. 3.3).

To connect this view of $\psi_{\max}(t)$ back to the streamfunction field itself, we estimate the mean overturning streamfunction as a function of latitude and depth, averaged separately over 1850–2000, well inside Regime A, and over 2225–2300, by which time the SSP5-8.5 trajectory has settled onto Regime B (Fig. 8). These are the first and last periods of Table 2, chosen as before so that neither average is contaminated by states acquired during the transition itself. SSP1-2.6 (top row), SSP5-3.4-OS (middle row) and SSP5-8.5 (bottom row) are drawn on a common colour scale; their historical panels are identical by construction, the historical record being common to the three runs, and are repeated so that each scenario can be read as a pair. SSP2-4.5, which ends in 2100, has no 2225–2300 average and is not shown. Under SSP5-8.5 the Regime B cell is visibly weaker and more compact than the Regime A cell, with a lower maximum streamfunction and no secondary cell of comparable strength. The difference between the two panels is therefore not one of amplitude alone. A circulation that had simply weakened would show the Regime A pattern scaled down, with the same cells in the same places and the same relative strengths; what the Regime B panel shows instead is a cell of different extent in both latitude and depth, and a secondary cell that has not merely weakened but effectively disappeared. The overturning of Regime B is thus organised differently from that of Regime A, which is what one expects if the two are distinct attractors rather than two points on a single one, and it is consistent with both the reduced $\psi_{\max}(t)$ and the lower ESS local dimension already documented for this scenario: fewer active degrees of freedom, and a spatial structure with fewer distinct components to support them. Under SSP1-2.6, by contrast, the late cell keeps the historical

https://doi.org/10.5194/egusphere-2026-6552
Preprint. Discussion started: 13 November 2026
© Author(s) 2026. CC BY 4.0 License.

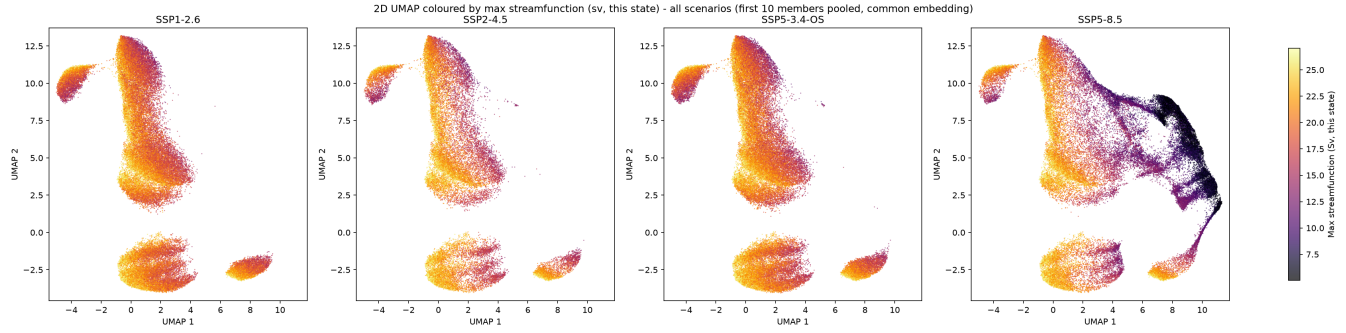


Figure 7. Multi-member UMAP embedding as Fig. 3, coloured here by maximum overturning current $\psi_{\max}(t)$ (Sv).

pattern: weaker, but with the same cells in the same places and the same relative strengths. That is what a purely quantitative decline looks like, and it is what SSP5-8.5 does not show. SSP5-3.4-OS behaves like SSP1-2.6: its late cell keeps the historical pattern, and its $\psi_{\max}$ over 2225–2300, 20.12 Sv, is if anything slightly closer to the historical 22.53 Sv than under SSP1-2.6 (19.66 Sv; Table 2). It is also interesting to note that these streamfunctions are virtually identical to what is obtained from idealised, but rather realistic, 2D latitude-depth model of the AMOC for the two stable steady states of the AMOC (Sévellec and Fedorov, 2011).

Together, these quantitative changes in a range of indices (colourings of Figs. 5, 6, and 7) and the significant changes of the AMOC (Fig. 8) motivate the independent confirmation that follows.

4.2 Local dimension confirms a graded, scenario dependent response

The ESS local dimension series for the historical run and its four scenario continuations are computed with no reference to the UMAP embedding of Sect. 4.1 (Fig. 9). To summarise them compactly we use three periods throughout the rest of this section: 1850–2000 (historical, common to all scenarios), 2030–2175 and 2225–2300. The periods were chosen by inspection of both the UMAP embedding (Sect. 4.1) and the $\hat{d}$ series (Fig. 9): over the first and last periods the system appears roughly stationary, while the second covers the transition between them, in the scenarios that undergo one. The periods are therefore not contiguous. The two intervals left out, 2000–2030 and 2175–2225, are those in which the trajectory is leaving one of these stages or entering the next, so that no period mixes states from two different stages of the response. We particularly focus on a few indices (Table 2): the mean and variance of $\hat{d}$, of the phase space velocity v (Sect. 4.3), and of the maximum overturning current $\psi_{\max}$ over each period, taken across all months and all ten members. In the simulations, SSP2-4.5 ends in 2100, so its second period covers 2030–2100 and its third is empty. For SSP5-3.4-OS the second period does not cover a transition but the excursion and the return together, the concentration peaking within it.

https://doi.org/10.5194/egusphere-2026-6552
Preprint. Discussion started: 13 November 2026
© Author(s) 2026. CC BY 4.0 License.

Table 2. Mean and variance of the ESS local dimension $\hat{d}$, the phase space velocity v and the maximum overturning current $\psi_{\max}$, by period and scenario. Statistics are computed over every month of the period and all ten ensemble members jointly, so that the variance reflects both the month to month and the inter-member spread. The 1850–2000 period lies within the common historical record, evaluated separately under each scenario's neighbour catalogue (Sect. 3.2). The first and last periods are those over which the system appears roughly stationary, and the second covers the transition; the intervals between them, 2000–2030 and 2175–2225, are excluded. SSP2-4.5 ends in 2100, so its second period covers 2030–2100 and its third is unavailable (—).

		$\hat{d}$		v (Sv month^{-1})		$\psi_{\max}$ (Sv)	
Period	Scenario	Mean	Var.	Mean	Var.	Mean	Var.
1850–2000	SSP1-2.6	22.49	8.208	2.842	1.113	22.53	5.437
	SSP2-4.5	22.33	8.150	2.842	1.113	22.53	5.437
	SSP5-3.4-OS	22.56	8.170	2.842	1.113	22.53	5.437
	SSP5-8.5	22.35	8.090	2.842	1.113	22.53	5.437
2030–2175	SSP1-2.6	22.87	8.283	2.717	0.9504	18.08	4.799
	SSP2-4.5*	19.12	6.565	2.690	0.9525	16.38	4.155
	SSP5-3.4-OS	21.98	7.838	2.680	0.9338	17.80	6.376
	SSP5-8.5	18.02	5.775	2.476	0.7161	13.53	7.410
2225–2300	SSP1-2.6	23.22	8.955	2.720	0.9642	19.66	5.180
	SSP2-4.5	—	—	—	—	—	—
	SSP5-3.4-OS	22.78	7.751	2.718	0.9622	20.12	6.059
	SSP5-8.5	21.37	7.294	2.127	0.4135	6.194	1.701

* 2030–2100.

4.2.1 The historical baseline and its sensitivity to the catalogue

Throughout the historical period the local dimension fluctuates around a stationary baseline of $\hat{d} \approx 22.33$–22.56, with a variance of about 8.1–8.2. This is *Regime A*, the attractor the model samples before any scenario specific forcing.

The results from the four scenarios (rows of Table 2) are close but not identical over this period (22.49, 22.33, 22.56 and 22.35), even though the underlying historical data are the same in all four cases. This is not a numerical artefact, and it is worth being explicit about, because it follows directly from the global neighbour search of Sect. 3.2. The k neighbours used to estimate $\hat{d}$ at a historical month are drawn from the entire catalogue of the run and need not be historical states themselves. A month in 1930 whose circulation happens to resemble a month in 2200 will take that future month into its neighbourhood, and since each scenario contributes a different set of post-2015 states to its own catalogue, the neighbourhoods of the shared historical months, and so their dimension estimates, differ slightly between scenarios.

https://doi.org/10.5194/egusphere-2026-6552
Preprint. Discussion started: 13 November 2026
© Author(s) 2026. CC BY 4.0 License.

What matters is the size of the effect. The four historical values agree to within 0.23, or $1\,\%$, whereas the scenario differences documented below reach 4 dimension units, roughly $19\,\%$. The estimator's sensitivity to the composition of the catalogue is thus more than an order of magnitude smaller than the signal we extract from it. It also indicates, incidentally, that few historical neighbourhoods contain future states at all, which is itself consistent with the historical and post-transition circulations occupying largely distinct regions of phase space.

4.2.2 Scenario responses after the 2015 branch point

After the 2015 branch point the four continuations diverge, mirroring the geometry of Sect. 4.1. Under SSP5-8.5, $\hat{d}$ falls from the Regime A baseline to 18.02 over 2030–2175, a reduction of some $19\,\%$, and its variance contracts to 5.78, about $71\,\%$ of the historical value. Over this period the circulation is therefore both lower dimensional and less variable in its dimensionality than it was historically, which is what one expects of a trajectory confined to a comparatively narrow passage of state space. This period coincides in time with the narrow corridor seen in the UMAP embedding, and we read it, as before, not as a third attractor but as a *transition corridor*: a dynamically constrained pathway the system must traverse between Regime A and Regime B. A possible physical reading of this lower dimension is that the dynamics in the corridor are both constrained and transitory. They are constrained because, while the forcing pushes the circulation out of Regime A, its evolution is dominated by a single coherent process: the forced weakening of the overturning cell under the warming and freshening of the subpolar North Atlantic, reinforced by the salt advection feedback (Stommel, 1961). The remaining degrees of freedom are then slaved to this slow, large scale adjustment rather than fluctuating independently. Theory leads one to expect exactly this close to a loss of stability: the dynamics collapse onto the few directions of the weakly damped mode, along which the variability concentrates, while all other directions remain strongly damped. They are transitory because the corridor is not an attractor the system samples repeatedly but a passage it crosses once. The states found there are spread along the direction of travel more than across it, so the neighbourhoods seen by the estimator are elongated and thin, and they engage fewer effective directions than those of a region the trajectory revisits in all directions. Both readings are consistent with the contraction of the variance of $\hat{d}$ over the same period. Both remain hypotheses that a process based analysis of the ocean fields would have to test.

Over the final period, 2225–2300, $\hat{d}$ recovers only partially, to 21.37. That is still some $4\,\%$ below the Regime A baseline, and it is sustained at that reduced level through to 2300 with no sign of a further recovery. This is *Regime B*. That its local dimension settles below the Regime A value rather than reverting to it is independent evidence, obtained without any dimensionality reduction, for a lasting change in the geometry of the attractor, and it corroborates what the embedding shows for this scenario (Fig. 3). The variance of $\hat{d}$ behaves in the same way: having contracted to 5.78 within the corridor, it recovers to 7.29 over the final period, still below the historical 8.09. Regime B is thus both lower dimensional and less variable in its dimensionality than Regime A, though by a smaller margin than the corridor itself, so that the dimensional signature of this scenario is most pronounced during the transition rather than after it. A possible physical explanation for the lower dimension of Regime B, and for its lower phase space velocity (Sect. 4.3), is that it is a less energetic, and therefore less complex, state of the circulation. With an overturning reduced to about 6 Sv (Table 2), the northward transport of heat and salt is much weaker. The warmer, fresher surface layer of the subpolar North Atlantic stabilises the water column and suppresses deep convection, which in

https://doi.org/10.5194/egusphere-2026-6552
Preprint. Discussion started: 13 November 2026
© Author(s) 2026. CC BY 4.0 License.

Regime A is a major source of variability of the overturning, in line with the deep mixing collapse found in other CMIP6 projections (Drijfhout et al., 2025). The primary cell also almost vanishes (Fig. 8). Fewer active processes, coupled more weakly, leave fewer independent ways for the streamfunction to vary: the dynamics engage fewer degrees of freedom, and they evolve more slowly and more regularly. In this reading, Regime B is not only a weaker overturning but a circulation with less energy available to sustain variability, consistent with the weak AMOC state of idealised models (Sévellec and Fedorov, 2011).

The gradual decrease of $\hat{d}$ as the trajectory enters the corridor, and its gradual increase as it leaves it (Fig. 9), should not be read entirely as a gradual change of the dynamics. Part of these slopes follows from the way the estimator works. $\hat{d}$ at a given state is computed from its $k = 50$ nearest neighbours (Sect. 3.2), and for a state close to the border between the corridor and one of the two attractors, these neighbours may lie partly in the corridor and partly in the attractor. The resulting estimate is then an average of the dimensions of the two regions, weighted by how many neighbours each contributes. Even an abrupt change of dimension at the entrance or exit of the corridor would therefore appear in $\hat{d}(t)$ as a smoother transition, spread over the months during which neighbourhoods straddle the border. The sharpness of the entrance and exit is thus a lower bound on what our estimates can resolve, not a measured property of the transition.

Under SSP1-2.6 the picture is quite different. $\hat{d}$ shows no systematic reduction at any point: it is 22.87 over 2030–2175 and 23.22 over 2225–2300, in both cases marginally *above* the historical baseline of 22.49 rather than below it, with a variance (8.28, then 8.96) that stays close to its historical value of 8.21. The excursion this scenario undergoes in the UMAP embedding is therefore not accompanied by any lasting loss of effective degrees of freedom. By the end of the simulation the circulation samples an attractor whose local dimension is indistinguishable from, if anything slightly richer than, the one it occupied before 2015. This is direct, independent evidence that the SSP1-2.6 excursion is transient and reversible, with no lasting change of attractor and no collapse.

SSP5-3.4-OS sits between the two over 2030–2175, and joins SSP1-2.6 afterwards. Over 2030–2175, $\hat{d}$ falls slightly, to 21.98, some 3 % below its historical baseline of 22.56, with a variance of 7.84, 96 % of its historical value. This is a reduction that SSP1-2.6 does not show at all, consistent with the trajectory having first followed SSP5-8.5 further along the pathway out of Regime A. It is, however, a small fraction of the SSP5-8.5 reduction over the same period (18.02, 19 % below baseline), and it comes with no contraction of the variance comparable to that of the SSP5-8.5 corridor (5.78). This period averages the excursion and the return, so the reduction at the height of the excursion is presumably somewhat larger than the period mean suggests; even so, the circulation does not enter the low dimensional corridor. Over 2225–2300, $\hat{d} = 22.78$, some 1 % *above* the historical baseline, with a variance of 7.75 close to its historical 8.17: as under SSP1-2.6, the circulation ends the simulation on an attractor whose local dimension is indistinguishable from the historical one. This is independent evidence that the overshoot is reversible in this model. A temporary exposure to the high forcing trajectory, followed by a decline of the concentration, leaves no lasting change of attractor; in this sense the overshoot is a safe one.

SSP2-4.5 offers no post-transition period to examine, since it stops in 2100. Over the one period available after the branch point (2030–2100) it gives $\hat{d} = 19.12$, some 14 % below its historical baseline of 22.33, with a variance reduced to 6.57, 81 % of its historical value. Both the sign and the magnitude of this change match what SSP5-8.5 does over its own corridor period (18.02, 19 % below baseline, variance 5.78), and the slightly smaller reduction is consistent with the weaker forcing of this

https://doi.org/10.5194/egusphere-2026-6552
Preprint. Discussion started: 13 November 2026
© Author(s) 2026. CC BY 4.0 License.

pathway. The time series (Fig. 9) shows that the drop sets in soon after 2015, as it does under SSP5-8.5, and persists to the end of the record with no sign of recovery. We read this as SSP2-4.5 having entered the same transition corridor by 2100. Its destination cannot be observed in these simulations, but we expect the circulation to settle, as under SSP5-8.5, onto a different attractor rather than to recover toward Regime A. Two observations support this expectation. First, the only other scenario to enter the corridor, SSP5-8.5, crosses it to Regime B, while the two that return to Regime A, SSP1-2.6 and SSP5-3.4-OS, show no comparable reduction of $\hat{d}$ at any stage; within this ensemble, entering the corridor and returning to Regime A never go together. Second, the contrast with SSP5-3.4-OS suggests that what decides entry into the corridor is the persistence of the forcing rather than its level at a given time. SSP5-3.4-OS is exposed to the same trajectory as SSP5-8.5 until 2040 and reaches a higher concentration than SSP2-4.5 by mid-century, yet its $\hat{d}$ over 2030–2175 falls by only $3\,\%$, because its concentration declines thereafter; SSP2-4.5, whose concentration keeps rising through 2100, loses $14\,\%$. The two periods are not identical, the SSP5-3.4-OS one extending to 2175 and so including its return, and restricting both to 2030–2100 would sharpen this comparison. We state the fate of SSP2-4.5 as an expectation rather than a result: confirming it would require simulations of this scenario beyond 2100.

The ESS local dimension is computed directly in the 540-dimensional phase space, with no dimensionality reduction, so it rests on mathematical machinery entirely unrelated to the UMAP embedding. Yet the two agree scenario by scenario: a lasting migration to a new attractor under SSP5-8.5, a migration that has entered the transition corridor by the end of the record under SSP2-4.5, and transient, fully reversible excursions under SSP1-2.6 and SSP5-3.4-OS, the latter larger but reversed all the same. This agreement extends to the graded structure of each scenario's response, not merely to a transition/no transition verdict. It is therefore much harder to explain away as an artefact of the UMAP projection than a claim resting on the embedding alone, and it rules out a purely quantitative, for instance linear, weakening of the circulation as an alternative explanation. We therefore treat the scenario dependent behaviour of Sect. 4.1 as a genuine, corroborated feature of the simulated AMOC dynamics.

4.3 Phase space velocity reveals a scenario dependent slowing down

As a further independent check on the picture established above, we use the phase space velocity $v(t)$ (Sect. 3.3) for the historical run and its four scenario continuations (Fig. 10). As with the ESS local dimension series (Fig. 9), each series is the average over the ten ensemble members; the corresponding period statistics are summarised in Table 2.

4.3.1 The historical baseline

Throughout the historical period v fluctuates around a stationary baseline of 2.84 Sv month^{-1}, with a variance of 1.113, and this baseline is identical across all four scenarios. It must be: the historical data are common to the four runs, and v (Sect. 3.3) involves no scenario dependent scaling. Unlike $\hat{d}$, whose estimate depends on the catalogue it is evaluated against, v is computed pointwise along each trajectory, so its agreement over the historical period checks the bookkeeping rather than the diagnostic.

https://doi.org/10.5194/egusphere-2026-6552
Preprint. Discussion started: 13 November 2026
© Author(s) 2026. CC BY 4.0 License.



4.3.2 Scenario responses after 2015

After 2015 the scenarios separate, broadly in the same order as the local dimension does, with one exception, SSP2-4.5, discussed below. Under SSP5-8.5 the decline is large and progressive: v falls to 2.476 Sv month^{-1} over 2030–2175, some 13 % below the historical baseline, and then to 2.127 over 2225–2300, fully 25 % below it. The variance falls faster still, from 1.113 historically to 0.716 and then 0.414, so that by the final period the month to month spread of the velocity is 37 % of its historical value, a reduction of nearly two thirds. The reorganised circulation of Regime B therefore does not merely occupy a different region of state space (Fig. 3) and support fewer effective degrees of freedom (Fig. 9); it also evolves distinctly more slowly, and far more regularly, than the pre-2015 circulation did. The maximum overturning current over the same periods corroborates this (Table 2), falling from 22.53 Sv historically to 13.53 Sv over 2030–2175 and 6.19 Sv over 2225–2300, a weakening of 73 %. A circulation that moves more slowly through phase space, explores fewer directions and sustains a weaker overturning cell is not simply in a different configuration; by every measure available to us it is genuinely less active.

Under SSP1-2.6 the reduction is present but small, and it does not deepen. v settles at 2.717 Sv month^{-1} over 2030–2175 and 2.720 Sv month^{-1} over 2225–2300, some 4 % below the historical baseline in both periods, with a variance (0.950, then 0.964 Sv^2 month^{-2}) that stays at 85–87 % of its historical value. A residual slowing of a few percent is thus not entirely absent under low forcing, and we do not claim otherwise. But it is roughly a sixth of the SSP5-8.5 reduction; it stabilises rather than continuing to grow once the concentration has peaked and begun to decline; and it comes with no contraction of the variance comparable to the SSP5-8.5 case. Taken with the local dimension, which under this scenario returns to and marginally exceeds its historical level, the picture is of a circulation that has been perturbed but not restructured.

SSP5-3.4-OS behaves almost exactly like SSP1-2.6. Over 2030–2175 its velocity, 2.680 Sv month^{-1}, is some 6 % below the historical baseline, marginally below SSP1-2.6's 2.717 Sv month^{-1} and well above SSP5-8.5's 2.476 Sv month^{-1}; its variance, 0.934 Sv^2 month^{-2}, is likewise close to SSP1-2.6's (0.950 Sv^2 month^{-2}) and well above SSP5-8.5's (0.716 Sv^2 month^{-2}). Over 2225–2300 it is indistinguishable from SSP1-2.6: 2.718 Sv month^{-1} with a variance of 0.962 Sv^2 month^{-2}, against 2.720 and 0.964. The larger excursion this scenario undergoes thus leaves only a faint trace in the pace of the dynamics while it lasts, and none once the forcing has declined. Among the three scenarios that reach 2300, the ordering over 2030–2175 is the same for v as for $\hat{d}$, SSP1-2.6, then SSP5-3.4-OS, then SSP5-8.5; but the SSP5-3.4-OS departure from SSP1-2.6 is small in both, compared with the gap that separates both from SSP5-8.5.

SSP2-4.5 is the exception, and again only one post-branch period is available. Over 2030–2100 its velocity, 2.690 Sv month^{-1}, is essentially indistinguishable from those of SSP1-2.6 (2.717 Sv month^{-1}) and SSP5-3.4-OS (2.680 Sv month^{-1}) and well above SSP5-8.5's (2.476 Sv month^{-1}), and its variance, 0.953 Sv^2 month^{-2}, is likewise almost identical to SSP1-2.6's (0.950 Sv^2 month^{-2}) and well above SSP5-8.5's (0.716 Sv^2 month^{-2}). The two diagnostics therefore rank this scenario differently: its local dimension has already dropped nearly to the SSP5-8.5 value, while its velocity has barely moved from the SSP1-2.6 value. We do not read this as a contradiction of the transition we expect for this scenario. The two quantities measure different things, a change in the geometry of the local neighbourhood as against the pace at which the state traverses it, and there is no reason for them to respond on the same timescale. Under SSP5-8.5 itself, $\hat{d}$ drops by 19 % over the corridor

https://doi.org/10.5194/egusphere-2026-6552
Preprint. Discussion started: 13 November 2026
© Author(s) 2026. CC BY 4.0 License.

period while v drops by only $13\,\%$, the largest reduction of v coming later, once Regime B is reached. If anything, this suggests that the dimensional signature of a transition emerges before the dynamical slowdown does, which would make $\hat{d}$ the more sensitive early indicator of the two, and SSP2-4.5 would then be a trajectory caught at the stage where the first has appeared and the second not yet. This rests on a single model, however, and would need testing against a wider ensemble before being relied on.

We read this scenario dependent slowdown as a direct phase space signature of the same underlying mechanism that classical scalar early warning indicators infer only indirectly, through the rising lag-1 autocorrelation of a single index (Boers, 2021; Ditlevsen and Ditlevsen, 2023). Under sustained high forcing (SSP5-8.5), both the mean pace of the circulation's evolution and the variability of that pace decline together once Regime B is established (2225–2300): $v(t)$ is lower on average and also less variable from month to month, so the post-transition circulation is not merely displaced to a different configuration but is, in this dynamical sense, less active overall. Under SSP1-2.6, by contrast, the forcing peaks around 2060 at a level too low to alter either the mean pace or its variability durably, and declines thereafter, consistent with the reversible character of this scenario's excursion already established from the UMAP embedding and the ESS local dimension (Sects. 4.1–4.2). The same holds under SSP5-3.4-OS, although its forcing follows the high emission trajectory until 2040 and peaks at a higher concentration: the decline that follows is enough for the pace and variability of the dynamics to return to the SSP1-2.6 values.

Read together with the maximum overturning current (Fig. 1), these diagnostics separate two things that a scalar index necessarily conflates. Under SSP5-8.5, $\psi_{\max}$ falls by $73\,\%$ between the historical period and 2225–2300, but the local dimension falls with it, to $4\,\%$ below baseline after passing through a corridor $19\,\%$ below it, and so does the phase space velocity, by $25\,\%$, with its variance reduced to $37\,\%$ of the historical value; the state also comes to occupy a region of the embedding disjoint from the historical cloud. The circulation of Regime B is thus weaker *and* differently organised. Under SSP1-2.6 the two come apart. That scenario's $\psi_{\max}$ over 2225–2300, 19.66 Sv, remains some $13\,\%$ below the historical 22.53 Sv, so it too ends the simulation with a measurably weaker overturning; yet $\hat{d}$ sits marginally *above* its historical baseline, v is within $4\,\%$ of it, and the trajectory has returned to Regime A. SSP5-3.4-OS tells the same story: its $\psi_{\max}$ over 2225–2300, 20.12 Sv, is some $11\,\%$ below the historical value, while its $\hat{d}$ is $1\,\%$ above baseline, its v is identical to that of SSP1-2.6, and its trajectory has returned to Regime A. A lasting weakening of the scalar index is therefore possible in these simulations with no accompanying change in the dynamics. That is direct evidence, internal to the ensemble, that the SSP5-8.5 response is not simply a larger version of the SSP1-2.6 one but a qualitatively different kind of response.

4.4 Relation to the CO_2 forcing

Having established the scenario dependent response with three independent diagnostics, we finally relate it to the forcing that drives it. Section 4.1.1 suggested that the four scenarios travel along a common pathway out of Regime A, at a pace set by the forcing, and the colouring of the embedding by the CO_2 concentration gave a first, qualitative test of this reading (Fig. 4). The barycentre distance $D(t)$ (Sect. 3.3) makes it quantitative. Figure 11 plots it against the prescribed CO_2 concentration, scenario by scenario. In all four scenarios $D(t)$ increases roughly linearly with the logarithm of the concentration, which is why the concentration axis of the figure is logarithmic: the higher the concentration, the further the centre of the cloud of states

https://doi.org/10.5194/egusphere-2026-6552
Preprint. Discussion started: 13 November 2026
© Author(s) 2026. CC BY 4.0 License.

lies from the historical one. The logarithm is the natural variable here, since the radiative forcing of CO_2 itself scales with the logarithm of its concentration (Myhre et al., 1998); a relation linear in the logarithm of the concentration is therefore, to a good approximation, a relation linear in the CO_2 forcing. The relation also holds as the concentration falls. Under SSP1-2.6 and SSP5-3.4-OS, $D(t)$ decreases again once the concentration has peaked, which is the reversibility seen in Fig. 3 expressed as a single number. That one quantity, the CO_2 content, accounts for most of the displacement across four different pathways indicates that it is the CO_2 forcing that drives the dynamics away from the original attractor.

Figure 12 shows the same relation for the conventional scalar index, the maximum overturning current $\psi_{\max}(t)$, so that the displacement of the state and the strength of the overturning can be read against the same forcing. $\psi_{\max}$ weakens as the concentration rises in all four scenarios: to first order, the scalar index is also set by the CO_2 content. Under SSP5-8.5 the relation steepens at the highest concentrations, departing from the roughly linear dependence on the logarithm of the concentration seen earlier on the pathway. Over 2175–2225 the overturning keeps weakening while the concentration, close to its peak, rises only slowly (Figs. 1 and 2), so that it loses more strength per unit of CO_2 than it did earlier on the same pathway; we return to this departure from a purely forcing driven decline in Sect. 5. Under SSP1-2.6 and SSP5-3.4-OS, $\psi_{\max}$ mostly recovers as the concentration declines. However there is still a mismatch, this is the lasting weakening of the scalar index, with no accompanying change in the dynamics, identified in Sect. 4.3. The forcing thus sets both the position of the state and the strength of the overturning to first order, but only the local dimension and the phase space velocity tell whether the weakening it causes comes with a change of regime. Hence, and despite the slight weakening of the AMOC post-2225, SSP1-2.6 and SSP5-3.4-OS trajectories are consistent with a safe overshoot (Ritchie et al., 2021), where the AMOC recovers its initial preindustrial regime.

5 Discussion and conclusions

The main outcome of this study is that two diagnostics built from unrelated mathematical machinery agree. The UMAP embedding is our exploratory tool for spotting a possible regime shift. Because embeddings of this kind can generate structure that comes from the projection algorithm rather than the data (Chari and Pachter, 2023; Kobak and Linderman, 2021), the ESS local dimension, computed directly in the un-projected 540-dimensional phase space, provides the corroborating check. The two agree not just on a binary transition/no transition verdict but scenario by scenario. That is a stronger basis for inferring a real dynamical response than either could give alone, and it complements the existing scalar index evidence for AMOC destabilisation (Rahmstorf et al., 2015; Boers, 2021; Ditlevsen and Ditlevsen, 2023) with a diagnostic that does not depend on the choice of a single summary index.

The response is graded rather than all-or-nothing. Under SSP5-8.5 the circulation crosses a low dimensional corridor and settles onto a distinct attractor by 2225–2300, with no sign of reverting. Under SSP1-2.6 it is displaced and then returns: by the end of the simulation its local dimension is indistinguishable from the historical value, with no lasting change of regime and no collapse. Under SSP5-3.4-OS it is displaced further, along the SSP5-8.5 pathway, but it returns in the same way, and by 2225–2300 its local dimension, phase space velocity and position in the embedding are those of SSP1-2.6. SSP2-4.5 ends in

https://doi.org/10.5194/egusphere-2026-6552
Preprint. Discussion started: 13 November 2026
© Author(s) 2026. CC BY 4.0 License.

2100, but by then its local dimension has dropped by $14\,\%$, close to the SSP5-8.5 corridor value, with no sign of a return: it has entered the corridor, and we expect it to settle onto a different attractor, although the record ends before this can be observed. That the outcome varies with the emission pathway is the result we would emphasise. Establishing whether it reflects a forced response or an unconditional bifurcation would require pathways and models beyond the single ensemble analysed here, and we note that this is a single model (ACCESS) study, carrying the structural biases in AMOC-relevant processes common to CMIP class ocean models. The AMOC response to high forcing differs markedly between CMIP6 models, from a persistent weakened circulation (Baker et al., 2025) to a shutdown after 2100 (Drijfhout et al., 2025), so the Regime B reached under SSP5-8.5 here need not be reached by other models; the diagnostics used here could be applied to them directly.

It is worth stating explicitly what this adds to the scalar picture. Under SSP5-8.5 the maximum overturning current falls by $73\,\%$ between the historical period and 2225–2300, a weakening of exactly the kind scalar index analyses are designed to detect (Rahmstorf et al., 2015; Boers, 2021; Ditlevsen and Ditlevsen, 2023). Our diagnostics indicate that this weakening is not the whole of the response. A purely quantitative decline, the same circulation running more slowly, would displace the state along the attractor it already occupied and would leave the local geometry of that attractor, and so $\hat{d}$, broadly unchanged. That is not what these simulations do. The trajectory leaves Regime A for a region of state space disjoint from it; the local dimension settles about $4\,\%$ below its historical value after a still more constrained passage $19\,\%$ below it; the phase space velocity declines by $25\,\%$ and becomes markedly more regular; and the mean overturning cell of Regime B is not a scaled down copy of the historical one but a more compact structure lacking a secondary cell of comparable strength (Fig. 8, consistent with theoretically expected AMOC weak-state, e.g., Sévellec and Fedorov, 2011). Under high forcing, then, our results suggest not merely a weakening of the AMOC but a dynamical reorganisation of it: by the end of the simulation the circulation differs from the historical one in the number of degrees of freedom it engages, and in the pace and regularity with which it evolves, and not only in its strength. SSP1-2.6 and SSP5-3.4-OS sharpen the distinction further, since they end with persistent weakenings of some $13\,\%$ and $11\,\%$ on the scalar index and yet no dimensional or velocity signature whatever. Weakening and reorganisation are therefore separable in these data, and a diagnostic built on circulation strength alone cannot by construction tell the two apart.

The overshoot pathway deserves a separate comment, because it bears directly on a question of policy relevance: whether a temporary exceedance of a forcing level, followed by its reversal, is safe for the AMOC. In these simulations it is. SSP5-3.4-OS is exposed to the high emission trajectory until 2040 and reaches a higher concentration than SSP1-2.6, yet its circulation stays within the basin of attraction of Regime A and returns to it; no lasting change is detected by any of our diagnostics, beyond a partial weakening of the scalar index shared with SSP1-2.6. Two caveats bound this conclusion. It is a single model result, and it concerns one overshoot pathway: the trajectory under SSP5-3.4-OS never enters the low dimensional corridor that SSP5-8.5 crosses, so it tells us that this overshoot is safe, not how large or how long an overshoot could be before it ceases to be. What it does provide is a bracket. The boundary of the basin of attraction of Regime A, if the pathway out of it has one, lies beyond the states reached under SSP5-3.4-OS and before those reached under SSP5-8.5 when its concentration levelled off. Pathways that cross the region between the two, with larger or later overshoots, are the natural next step for locating that boundary. SSP2-4.5 also bears on this question. By 2100 it has entered the corridor that SSP5-3.4-OS never reaches, although its concentration is

https://doi.org/10.5194/egusphere-2026-6552
Preprint. Discussion started: 13 November 2026
© Author(s) 2026. CC BY 4.0 License.

lower than that of SSP5-3.4-OS at mid-century. This suggests that the duration of the forcing, and not only its peak, matters for whether the basin of attraction of Regime A is left; the absence of a decline in the forcing of SSP2-4.5 before 2100 is what separates it from the overshoot pathway. An extension of SSP2-4.5 beyond 2100 would both test our expectation that it tips and help locate the basin boundary.

We read the dimension change itself conservatively. The reduction in $\hat{d}$ under SSP5-8.5 indicates that the circulation of Regime B is dynamically less complex than the historical one, with the transition corridor the most constrained stage of all; the phase space velocity and the maximum overturning current decline over the same interval, so a simpler attractor goes together with a slower and weaker circulation. Our diagnostics cannot by themselves establish which aspects of the circulation account for this. We have suggested two candidate explanations (Sect. 4.2.2). In the corridor, the dynamics would be both constrained, slaved to the forced weakening of the overturning, and transitory, crossed once rather than revisited. In Regime B, the circulation would be less energetic, with suppressed deep convection and almost no primary cell leaving fewer active processes. Testing these explanations would require a process based analysis of the underlying ocean fields, for instance of convective activity and of the heat and salt budgets of the subpolar North Atlantic along the pathway.

The barycentre distance gives the forcing its place in this picture. Across the four scenarios, the distance of the state from the historical attractor grows roughly linearly with the logarithm of the CO_2 concentration, and so with the CO_2 radiative forcing, and under SSP1-2.6 and SSP5-3.4-OS it shrinks again as the concentration declines (Fig. 11). To first order, then, it is the CO_2 content that pushes the circulation away from Regime A. The maximum overturning current follows the concentration in the same way (Fig. 12), but under SSP1-2.6 and SSP5-3.4-OS it remains weaker than historically once the concentration has declined, whereas the dynamics have recovered. This suggests that, despite the slight weakening of the recovered AMOC, SSP1-2.6 and SSP5-3.4-OS are safe overshoot pathways (Ritchie et al., 2021), where the preindustrial AMOC dynamical regime is recovered. The forcing does not account for everything, however.

This internal reorganisation of the system is also supported by the unique evolution of the AMOC between 2175 and 2225 (Fig. 1, 9, 12), a period during which a more pronounced decline is observed while the rate of increase in forcing is already slowing down (Fig. 2). This appears to contradict the idea of a purely forcing-driven decline in the circulation.

Taken together, these results indicate that the choice of emission pathway is central to AMOC stability under this model's dynamics; that the displacement of the circulation from its historical attractor scales roughly linearly with the logarithm of the CO_2 concentration, that is, with its radiative forcing; that under the highest pathway the circulation is not merely weakened but dynamically reorganised, and that the intermediate pathway has entered the same reorganisation by 2100; that a temporary overshoot along that pathway, reversed from mid-century, is not; and that pairing an exploratory embedding with an independent local dimension diagnostic is a useful way to distinguish genuine dynamical regime shifts from projection artefacts in large geophysical datasets.

Nothing in these methods is specific to the AMOC, or to these simulations. It requires only a system whose state can be assembled into a high dimensional vector sampled repeatedly in time, and a question about whether that state has changed regime rather than merely changed magnitude. Other candidate tipping elements, atmospheric circulation regimes, and reanalysis or observational records of sufficient length all meet those conditions, as do forced ensembles from other models and

https://doi.org/10.5194/egusphere-2026-6552
Preprint. Discussion started: 13 November 2026
© Author(s) 2026. CC BY 4.0 License.

other experimental designs. Wherever the available evidence rests on scalar indices, and a reorganisation might therefore pass unrecorded because it leaves the chosen index largely unchanged (or changed, but not qualitatively, as in our AMOC study under SSP1-2.6 and SSP5-3.4-OS), the combination of an exploratory embedding with a corroborating diagnostic computed in the un-projected phase space offers a way to look for it directly.

Data availability. The ACCESS-ESM1.5 CMIP6 output used in this study (the `historical`, `ssp126`, `ssp245`, `ssp534-over` and `ssp585` experiments, variable `msftmz`) is publicly available through the Earth System Grid Federation (https://esgf-node.llnl.gov/search/cmip6/). The prescribed CO_2 concentrations are available from the input4MIPs archive (Meinshausen et al., 2020).

Author contributions. TC and FS designed the study, which was then refined through discussions among all three authors. TC developed the analysis code and performed the computations. All authors contributed equally to the analysis of the results and to the writing of the manuscript.

Competing interests. The authors declare that they have no conflict of interest.

Acknowledgements. AI tools were used to improve the grammar and sentence structure of the manuscript and to help format it and its reference list according to the journal template. The authors reviewed and edited all resulting text and take full responsibility for the content of the manuscript.

Financial support. TC was supported by ISblue project, Interdisciplinary graduate school for the blue planet (ANR-17-EURE-0015) and co-funded by a grant from the French government under the program "Investissements d'Avenir" embedded in France 2030. FS was supported by the PORC-EPIC project (ANR-24-CE56-4512) funded through the French ANR program. AC was supported by the Advanced Research + Invention Agency (ARIA) through the Forecasting Tipping Points programme, as part of the SORTED project.

https://doi.org/10.5194/egusphere-2026-6552
Preprint. Discussion started: 13 November 2026
© Author(s) 2026. CC BY 4.0 License.

References

Armstrong McKay, D. I., Staal, A., Abrams, J. F., Winkelmann, R., Sakschewski, B., Loriani, S., Fetzer, I., Cornell, S. E., Rockström, J., and Lenton, T. M.: Exceeding 1.5 °C global warming could trigger multiple climate tipping points, Science, 377, eabn7950, https://doi.org/10.1126/science.abn7950, 2022.

Baker, J. A., Bell, M. J., Jackson, L. C., Renshaw, R., Vallis, G. K., Watson, A. J., and Wood, R. A.: Overturning pathways control AMOC weakening in CMIP6 models, Geophys. Res. Lett., 50, e2023GL103381, https://doi.org/10.1029/2023GL103381, 2023.

Baker, J. A., Bell, M. J., Jackson, L. C., Vallis, G. K., Watson, A. J., and Wood, R. A.: Continued Atlantic overturning circulation even under climate extremes, Nature, 638, 987–994, https://doi.org/10.1038/s41586-024-08544-0, 2025.

Bi, D., Dix, M., Marsland, S., O'Farrell, S., Sullivan, A., Bodman, R., Law, R., Harman, I., Srbinovsky, J., Rashid, H. A., Dobrohotoff, P., Mackallah, C., Yan, H., Hirst, A., Savita, A., Dias, F. B., Woodhouse, M., Fiedler, R., and Heerdegen, A.: Configuration and spin-up of ACCESS-CM2, the new generation Australian Community Climate and Earth System Simulator Coupled Model, J. South. Hemisph. Earth Syst. Sci., 70, 225–251, https://doi.org/10.1071/ES19040, 2020.

Boers, N.: Observation-based early-warning signals for a collapse of the Atlantic Meridional Overturning Circulation, Nat. Clim. Change, 11, 680–688, https://doi.org/10.1038/s41558-021-01097-4, 2021.

Böhm, E., Lippold, J., Gutjahr, M., and Paquay, F.: Strong and deep Atlantic meridional overturning circulation during the last glacial cycle, Nature, 517, 73–76, https://doi.org/10.1038/nature14059, 2015.

Boulton, C. A., Allison, L. C., and Lenton, T. M.: Early warning signals of Atlantic Meridional Overturning Circulation collapse in a fully coupled climate model, Nat. Commun., 5, 5752, https://doi.org/10.1038/ncomms6752, 2014.

Caby, T., Faranda, D., Vaienti, S., and Yiou, P.: Extreme value distributions of observation recurrences, Nonlinearity, 34, 118–163, https://doi.org/10.1088/1361-6544/abaff1, 2021.

Caby, T., Pineau-Guillou, L., Sévellec, F., and Delouis, J. M.: Dynamical properties of atmospheric and sea level extremes in the North-East Atlantic, Clim. Dynam., 64, 20, https://doi.org/10.1007/s00382-025-08008-9, 2026.

Caesar, L., Rahmstorf, S., Robinson, A., Feulner, G., and Saba, V.: Observed fingerprint of a weakening Atlantic Ocean overturning circulation, Nature, 556, 191–196, https://doi.org/10.1038/s41586-018-0006-5, 2018.

Campadelli, P., Casiraghi, E., Ceruti, C., and Rozza, A.: Intrinsic dimension estimation: relevant techniques and a benchmark framework, Math. Probl. Eng., 2015, 759567, https://doi.org/10.1155/2015/759567, 2015.

Chari, T. and Pachter, L.: The specious art of single-cell genomics, PLoS Comput. Biol., 19, e1011288, https://doi.org/10.1371/journal.pcbi.1011288, 2023.

Coquereau, A., Sévellec, F., Huck, T., Hirschi, J. J.-M., and Jamet, Q.: Past, present, and future variability of Atlantic meridional overturning circulation in CMIP6 ensembles, Earth Syst. Dynam., 17, 209–233, https://doi.org/10.5194/esd-17-209-2026, 2026.

Dansgaard, W., Johnsen, S. J., Clausen, H. B., and Bond, G.: Evidence for general instability of past climate from a 250-kyr ice-core record, Nature, 364, 218–220, https://doi.org/10.1038/364218a0, 1993.

del Amo, I., Datseris, G., and Holland, M.: Limitations of estimating local dimension and extremal index using exceedances in dynamical systems, Chaos, 35, 043128, https://doi.org/10.1063/5.0250492, 2025.

Ditlevsen, P. and Ditlevsen, S.: Warning of a forthcoming collapse of the Atlantic meridional overturning circulation, Nat. Commun., 14, 4254, https://doi.org/10.1038/s41467-023-39810-w, 2023.

https://doi.org/10.5194/egusphere-2026-6552
Preprint. Discussion started: 13 November 2026
© Author(s) 2026. CC BY 4.0 License.



Drijfhout, S., Angevaare, J. R., Mecking, J., van Westen, R. M., and Rahmstorf, S.: Shutdown of northern Atlantic overturning after 2100 following deep mixing collapse in CMIP6 projections, Environ. Res. Lett., 20, 094062, https://doi.org/10.1088/1748-9326/adfa3b, 2025.

Eyring, V., Bony, S., Meehl, G. A., Senior, C. A., Stevens, B., Stouffer, R. J., and Taylor, K. E.: Overview of the Coupled Model Intercomparison Project Phase 6 (CMIP6) experimental design and organization, Geosci. Model Dev., 9, 1937–1958, https://doi.org/10.5194/gmd-9-1937-2016, 2016.

Faranda, D. and Vaienti, S.: Correlation dimension and phase space contraction via extreme value theory, Chaos, 28, 041103, https://doi.org/10.1063/1.5027386, 2018.

Faranda, D., Messori, G., and Yiou, P.: Dynamical proxies of North Atlantic predictability and extremes, Sci. Rep.-UK, 7, 41278, https://doi.org/10.1038/srep41278, 2017.

Faranda, D., Messori, G., Alberti, T., Alvarez-Castro, M. C., Caby, T., Cavicchia, L., Coppola, E., Donner, R. V., Dubrulle, B., Galfi, V. M., Holmberg, E., Lembo, V., Noyelle, R., Yiou, P., Spagnolo, B., Valenti, D., Vaienti, S., and Wormell, C.: Statistical physics and dynamical systems perspectives on geophysical extreme events, Phys. Rev. E, 110, 041001, https://doi.org/10.1103/PhysRevE.110.041001, 2024.

Fox-Kemper, B., Hewitt, H. T., Xiao, C., Aðalgeirsdóttir, G., Drijfhout, S. S., Edwards, T. L., Golledge, N. R., Hemer, M., Kopp, R. E., Krinner, G., Mix, A., Notz, D., Nowicki, S., Nurhati, I. S., Ruiz, L., Sallée, J.-B., Slangen, A. B. A., and Yu, Y.: Ocean, cryosphere and sea level change, in: Climate Change 2021: The Physical Science Basis. Contribution of Working Group I to the Sixth Assessment Report of the Intergovernmental Panel on Climate Change, edited by: Masson-Delmotte, V., Zhai, P., Pirani, A., Connors, S. L., Péan, C., Berger, S., Caud, N., Chen, Y., Goldfarb, L., Gomis, M. I., Huang, M., Leitzell, K., Lonnoy, E., Matthews, J. B. R., Maycock, T. K., Waterfield, T., Yelekçi, O., Yu, R., and Zhou, B., Cambridge University Press, Cambridge, UK and New York, NY, USA, 1211–1362, https://doi.org/10.1017/9781009157896.011, 2021.

Freitas, A. C. M., Freitas, J. M., and Todd, M.: Hitting time statistics and extreme value theory, Probab. Theory Rel., 147, 675–710, https://doi.org/10.1007/s00440-009-0221-y, 2010.

Fu, Y., Lozier, M. S., Biló, T. C., Bower, A. S., Cunningham, S. A., Cyr, F., de Jong, M. F., deYoung, B., Drysdale, L., Fraser, N., Fried, N., Furey, H. H., Han, G., Handmann, P., Holliday, N. P., Holte, J., Inall, M. E., Johns, W. E., Jones, S., Karstensen, J., Li, F., Pacini, A., Pickart, R. S., Rayner, D., Straneo, F., and Yashayaev, I.: Seasonality of the Meridional Overturning Circulation in the subpolar North Atlantic, Commun. Earth Environ., 4, 181, https://doi.org/10.1038/s43247-023-00848-9, 2023.

Ganachaud, A. and Wunsch, C.: Improved estimates of global ocean circulation, heat transport and mixing from hydrographic data, Nature, 408, 453–457, https://doi.org/10.1038/35044048, 2000.

Henry, L. G. and McManus, J. F.: North Atlantic ocean circulation and abrupt climate change during the last glaciation, Science, 353, 470–474, https://doi.org/10.1126/science.aaf5529, 2016.

Johns, W. E., Elipot, S., Smeed, D. A., Moat, B., King, B., Volkov, D. L., and Smith, R. H.: Towards two decades of Atlantic Ocean mass and heat transports at 26.5° N, Philos. T. R. Soc. A, 381, 20220188, https://doi.org/10.1098/rsta.2022.0188, 2023.

Johnsson, K., Soneson, C., and Fontes, M.: Low bias local intrinsic dimension estimation from expected simplex skewness, IEEE T. Pattern Anal., 37, 196–202, https://doi.org/10.1109/TPAMI.2014.2343220, 2015.

Kobak, D. and Linderman, G. C.: Initialization is critical for preserving global data structure in both t-SNE and UMAP, Nat. Biotechnol., 39, 156–157, https://doi.org/10.1038/s41587-020-00809-z, 2021.

Koman, G., Bower, A. S., Holliday, N. P., Furey, H. H., Fu, Y., and Biló, T. C.: Observed decrease in Deep Western Boundary Current transport in subpolar North Atlantic, Nat. Geosci., 17, 1148–1153, https://doi.org/10.1038/s41561-024-01555-6, 2024.

https://doi.org/10.5194/egusphere-2026-6552
Preprint. Discussion started: 13 November 2026
© Author(s) 2026. CC BY 4.0 License.



Lenton, T. M., Held, H., Kriegler, E., Hall, J. W., Lucht, W., Rahmstorf, S., and Schellnhuber, H. J.: Tipping elements in the Earth's climate system, P. Natl. Acad. Sci. USA, 105, 1786–1793, https://doi.org/10.1073/pnas.0705414105, 2008.

Levina, E. and Bickel, P. J.: Maximum likelihood estimation of intrinsic dimension, in: Advances in Neural Information Processing Systems 17 (NIPS 2004), MIT Press, Cambridge, MA, USA, 777–784, 2004.

Lucarini, V., Faranda, D., Freitas, A. C. M., Freitas, J. M., Holland, M., Kuna, T., Nicol, M., Todd, M., and Vaienti, S.: Extremes and Recurrence in Dynamical Systems, John Wiley & Sons, Hoboken, NJ, USA, https://doi.org/10.1002/9781118632321, 2016.

McInnes, L., Healy, J., and Melville, J.: UMAP: Uniform Manifold Approximation and Projection for dimension reduction, arXiv [preprint], https://doi.org/10.48550/arXiv.1802.03426, 2018.

McManus, J. F., Francois, R., Gherardi, J. M., and Keigwin, L. D.: Collapse and rapid resumption of Atlantic meridional circulation linked to deglacial climate changes, Nature, 428, 834–837, https://doi.org/10.1038/nature02494, 2004.

Meinshausen, M., Nicholls, Z. R. J., Lewis, J., Gidden, M. J., Vogel, E., Freund, M., Beyerle, U., Gessner, C., Nauels, A., Bauer, N., Canadell, J. G., Daniel, J. S., John, A., Krummel, P. B., Luderer, G., Meinshausen, N., Montzka, S. A., Rayner, P. J., Reimann, S., Smith, S. J., van den Berg, M., Velders, G. J. M., Vollmer, M. K., and Wang, R. H. J.: The shared socio-economic pathway (SSP) greenhouse gas concentrations and their extensions to 2500, Geosci. Model Dev., 13, 3571–3605, https://doi.org/10.5194/gmd-13-3571-2020, 2020.

Mercier, H., Lherminier, P., Sarafanov, A., Gaillard, F., Daniault, N., Desbruyères, D., Falina, A., Ferron, B., Gourcuff, C., Huck, T., and Thierry, V.: Variability of the meridional overturning circulation at the Greenland–Portugal OVIDE section from 1993 to 2010, Prog. Oceanogr., 132, 250–261, https://doi.org/10.1016/j.pocean.2013.11.001, 2015.

Mercier, H., Desbruyères, D., Lherminier, P., Velo, A., Carracedo, L., Fontela, M., and Pérez, F. F.: New insights into the eastern subpolar North Atlantic meridional overturning circulation from OVIDE, Ocean Sci., 20, 779–797, https://doi.org/10.5194/os-20-779-2024, 2024.

Moat, B. I., Smeed, D. A., Frajka-Williams, E., Desbruyères, D. G., Beaulieu, C., Johns, W. E., Rayner, D., Sanchez-Franks, A., Baringer, M. O., Volkov, D., Jackson, L. C., and Bryden, H. L.: Pending recovery in the strength of the meridional overturning circulation at 26° N, Ocean Sci., 16, 863–874, https://doi.org/10.5194/os-16-863-2020, 2020.

Moat, B. I., Smeed, D. A., Rayner, D., Johns, W. E., Smith, R., Volkov, D., Elipot, S., Petit, T., Kajtar, J., Baringer, M. O., and Collins, J.: Atlantic meridional overturning circulation observed by the RAPID-MOCHA-WBTS (RAPID-Meridional Overturning Circulation and Heatflux Array-Western Boundary Time Series) array at 26° N from 2004 to 2023 (v2023.1), NERC EDS British Oceanographic Data Centre NOC [data set], https://doi.org/10.5285/223b34a32dc5c945e0637086abc0f274, 2024.

Myhre, G., Highwood, E. J., Shine, K. P., and Stordal, F.: New estimates of radiative forcing due to well mixed greenhouse gases, Geophys. Res. Lett., 25, 2715–2718, https://doi.org/10.1029/98GL01908, 1998.

O'Neill, B. C., Tebaldi, C., van Vuuren, D. P., Eyring, V., Friedlingstein, P., Hurtt, G., Knutti, R., Kriegler, E., Lamarque, J.-F., Lowe, J., Meehl, G. A., Moss, R., Riahi, K., and Sanderson, B. M.: The Scenario Model Intercomparison Project (ScenarioMIP) for CMIP6, Geosci. Model Dev., 9, 3461–3482, https://doi.org/10.5194/gmd-9-3461-2016, 2016.

Platzer, P. and Chapron, B.: Density-induced variations of local dimension estimates for absolutely continuous random variables, J. Stat. Phys., 192, 34, https://doi.org/10.1007/s10955-025-03416-x, 2025.

Portmann, V., Swingedouw, D., Khattab, O., and Chavent, M.: Observational constraints project a ∼50 % AMOC weakening by the end of this century, Sci. Adv., 12, eadx4298, https://doi.org/10.1126/sciadv.adx4298, 2026.

Rahmstorf, S., Box, J. E., Feulner, G., Mann, M. E., Robinson, A., Rutherford, S., and Schaffernicht, E. J.: Exceptional twentieth-century slowdown in Atlantic Ocean overturning circulation, Nat. Clim. Change, 5, 475–480, https://doi.org/10.1038/nclimate2554, 2015.

https://doi.org/10.5194/egusphere-2026-6552
Preprint. Discussion started: 13 November 2026
© Author(s) 2026. CC BY 4.0 License.



Ritchie, P. D. L., Clarke, J. J., Cox, P. M., and Huntingford, C.: Overshooting tipping point thresholds in a changing climate, Nature, 592, 517–523, https://doi.org/10.1038/s41586-021-03263-2, 2021.

Rozza, A., Lombardi, G., Ceruti, C., Casiraghi, E., and Campadelli, P.: Novel high intrinsic dimensionality estimators, Mach. Learn., 89, 37–65, https://doi.org/10.1007/s10994-012-5294-7, 2012.

Sévellec, F. and Fedorov, A. V.: Stability of the Atlantic meridional overturning circulation and stratification in a zonally averaged ocean model: Effects of freshwater flux, Southern Ocean winds, and diapycnal diffusion, Deep-Sea Res. Pt. II, 58, 1927–1943, https://doi.org/10.1016/j.dsr2.2010.10.070, 2011.

Sévellec, F. and Fedorov, A. V.: Millennial variability in an idealised ocean model: predicting the AMOC regime shifts, J. Climate, 27, 3551–3564, https://doi.org/10.1175/JCLI-D-13-00450.1, 2014.

Sévellec, F. and Fedorov, A. V.: AMOC sensitivity to surface buoyancy fluxes: stronger ocean meridional heat transport with a weaker volume transport?, Clim. Dynam., 47, 1497–1513, https://doi.org/10.1007/s00382-015-2915-4, 2016.

Sévellec, F., Fedorov, A. V., and Liu, W.: Arctic sea-ice decline weakens the Atlantic meridional overturning circulation, Nat. Clim. Change, 7, 604–610, https://doi.org/10.1038/nclimate3353, 2017.

Stommel, H.: Thermohaline convection with two stable regimes of flow, Tellus, 13, 224–230, https://doi.org/10.1111/j.2153-3490.1961.tb00079.x, 1961.

Terhaar, J., Vogt, L., and Foukal, N. P.: Atlantic overturning inferred from air-sea heat fluxes indicates no decline since the 1960s, Nat. Commun., 16, 222, https://doi.org/10.1038/s41467-024-55297-5, 2025.

Trenberth, K. E. and Fasullo, J. T.: Atlantic meridional heat transports computed from balancing Earth's energy locally, Geophys. Res. Lett., 44, 1919–1927, https://doi.org/10.1002/2016GL072475, 2017.

van Westen, R. M., Kliphuis, M., and Dijkstra, H. A.: Physics-based early warning signal shows that AMOC is on tipping course, Sci. Adv., 10, eadk1189, https://doi.org/10.1126/sciadv.adk1189, 2024.

van Westen, R. M., Vanderborght, E., Kliphuis, M., and Dijkstra, H. A.: Physics-based indicators for the onset of an AMOC collapse under climate change, J. Geophys. Res.-Oceans, 130, e2025JC022651, https://doi.org/10.1029/2025JC022651, 2025.

Weijer, W., Cheng, W., Garuba, O. A., Hu, A., and Nadiga, B. T.: CMIP6 models predict significant 21st century decline of the Atlantic meridional overturning circulation, Geophys. Res. Lett., 47, e2019GL086075, https://doi.org/10.1029/2019GL086075, 2020.

Ziehn, T., Chamberlain, M. A., Law, R. M., Lenton, A., Bodman, R. W., Dix, M., Stevens, L., Wang, Y., and Srbinovsky, J.: The Australian Earth System Model: ACCESS-ESM1.5, J. South. Hemisph. Earth Syst. Sci., 70, 193–214, https://doi.org/10.1071/ES19035, 2020.

Zimmerman, C. C., Wagner, T. J. W., Maroon, E. A., and McNamara, D. E.: Slowed response of Atlantic meridional overturning circulation not a robust signal of collapse, Geophys. Res. Lett., 52, e2024GL112415, https://doi.org/10.1029/2024GL112415, 2025.

https://doi.org/10.5194/egusphere-2026-6552
Preprint. Discussion started: 13 November 2026
© Author(s) 2026. CC BY 4.0 License.

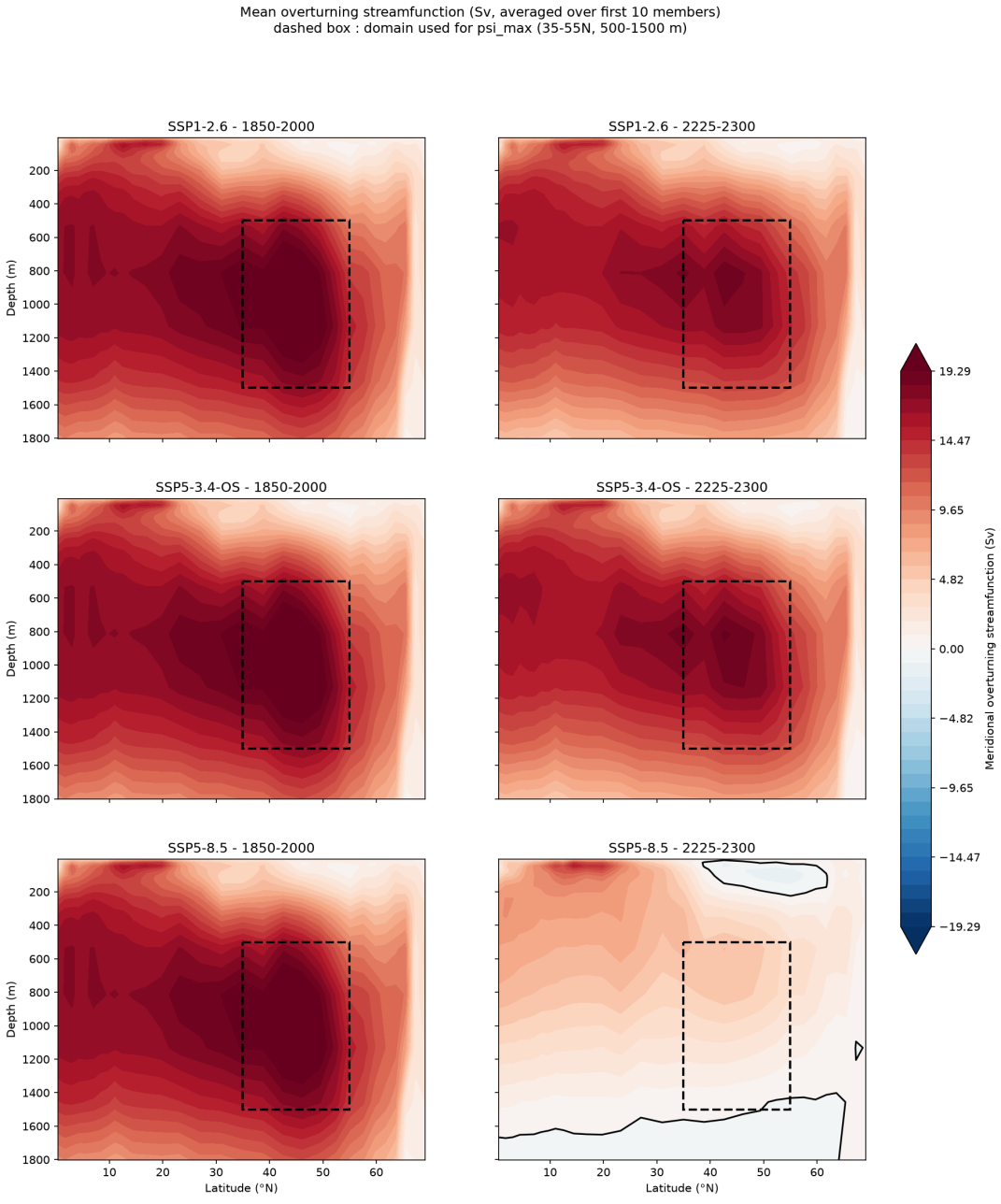


Figure 8. Mean AMOC overturning streamfunction (Sv) as a function of latitude and depth, averaged over the first ten ensemble members, for SSP1-2.6 (top row), SSP5-3.4-OS (middle row) and SSP5-8.5 (bottom row), over 1850–2000 (left, within the historical Regime A) and 2225–2300 (right, after the transition, within Regime B under SSP5-8.5). All six panels share one colour scale; the three historical panels are identical by construction, the historical record being common to the three runs. SSP2-4.5, which ends in 2100, has no 2225–2300 average and is not shown. The dashed box marks the subdomain over which $\psi_{\max}$ is computed (35–55°N, 500–1500 m; Sect. 3.3).

https://doi.org/10.5194/egusphere-2026-6552
Preprint. Discussion started: 13 November 2026
© Author(s) 2026. CC BY 4.0 License.

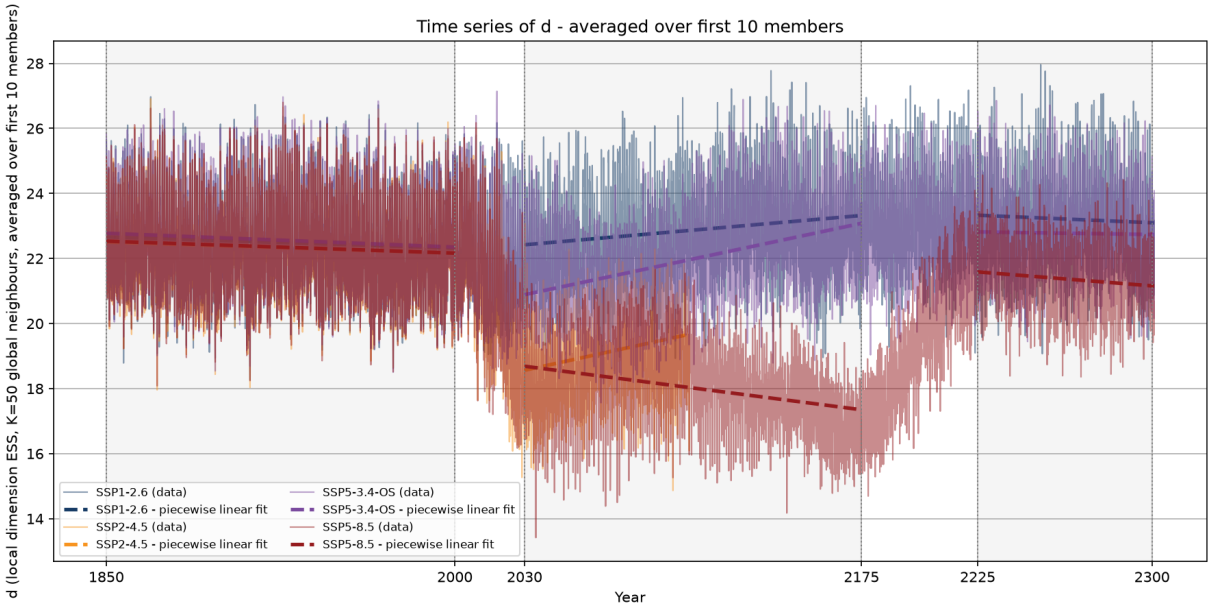


Figure 9. ESS local dimension $\hat{d}(t)$ of the AMOC streamfunction phase space for the historical run continued under SSP1-2.6 (dark blue), SSP2-4.5 (orange), SSP5-3.4-OS (purple) and SSP5-8.5 (dark red); SSP2-4.5 is available only to 2100, the three others extend to 2300. Each series is averaged over the first ten ensemble members. Dashed lines are linear fits over each of the three periods of Table 2 (1850–2000, 2030–2175 and 2225–2300, shaded).

https://doi.org/10.5194/egusphere-2026-6552
Preprint. Discussion started: 13 November 2026
© Author(s) 2026. CC BY 4.0 License.

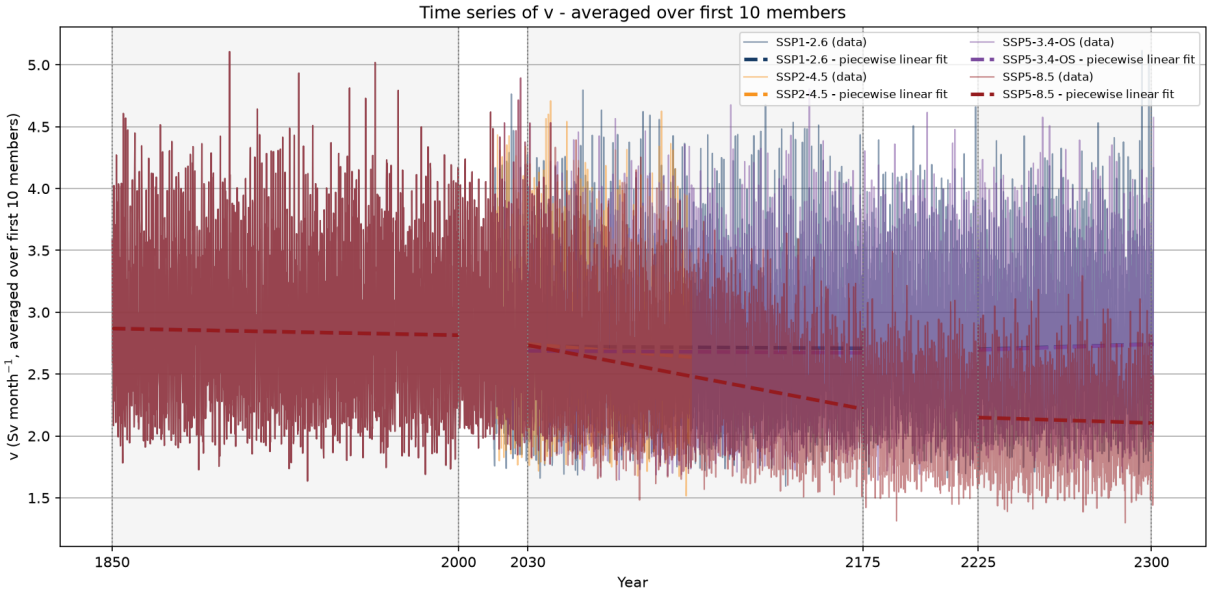


Figure 10. Phase space velocity $v(t)$ (Sect. 3.3) of the AMOC streamfunction trajectory for the historical run continued under SSP1-2.6 (dark blue), SSP2-4.5 (orange), SSP5-3.4-OS (purple) and SSP5-8.5 (dark red); SSP2-4.5 is available only to 2100, the three others extend to 2300. Averaged over the first ten ensemble members. Dashed lines are linear fits over each of the three periods of Table 2 (1850–2000, 2030–2175 and 2225–2300, shaded).

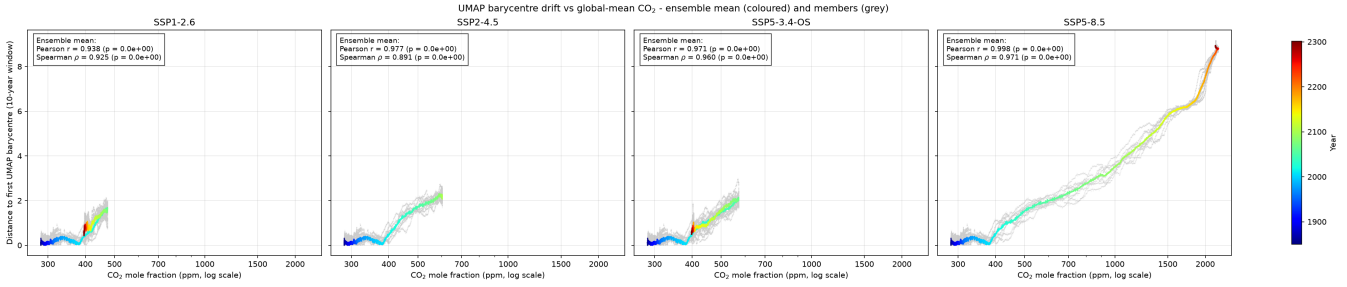


Figure 11. Distance $D(t)$ between the ten year sliding barycentre of the UMAP embedding (Fig. 3) and its first, 1850–1855 barycentre (Sect. 3.3), against the global mean atmospheric CO_2 concentration (ppm; Fig. 2), for SSP1-2.6, SSP2-4.5, SSP5-3.4-OS and SSP5-8.5, from left to right. The CO_2 axis is logarithmic. Coloured points: ensemble mean over the ten members, coloured by year; the barycentre of all ten members together. Grey points: each member separately; the barycentre of that member, against the same reference. Each panel gives the Pearson correlation between the ensemble mean and the logarithm of the concentration, and the Spearman rank correlation between the ensemble mean and the concentration, which is unaffected by the logarithmic transform.

https://doi.org/10.5194/egusphere-2026-6552
Preprint. Discussion started: 13 November 2026
© Author(s) 2026. CC BY 4.0 License.

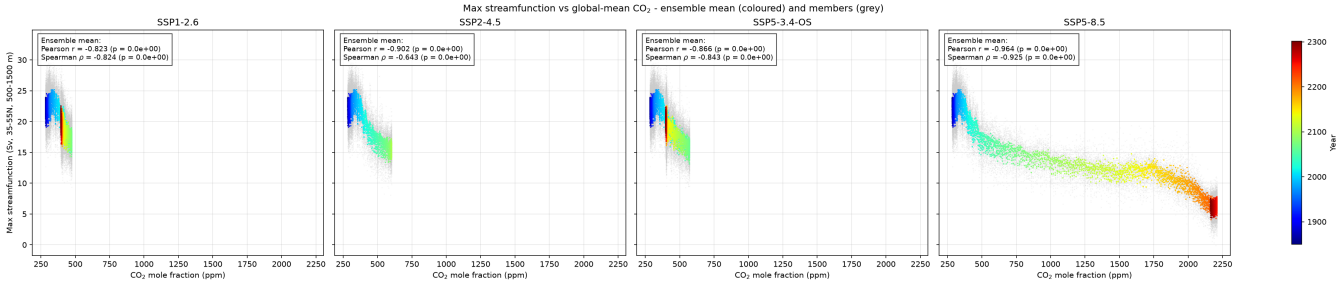


Figure 12. Maximum overturning current $\psi_{\max}(t)$ (Sv; Sect. 3.3) against the global mean atmospheric CO_2 concentration (ppm; Fig. 2), for SSP1-2.6, SSP2-4.5, SSP5-3.4-OS and SSP5-8.5, from left to right. The CO_2 axis is logarithmic. Coloured points: ensemble mean over the ten members, coloured by year. Grey points: each member separately. Each panel gives the Pearson correlation between the ensemble mean and the logarithm of the concentration, and the Spearman rank correlation between the ensemble mean and the concentration, which is unaffected by the logarithmic transform.